September 1985 LRP 275/85

GLOBAL WAVES IN COLD PLASMAS

L. Villard, K. Appert, R. Gruber and J. Vaclavik

Invited paper presented at the

3rd European Workshop on Problems in the Numerical Modeling of Plasmas
NUMOP 85

Varenna, Italy, 10 - 13 September 1985

GLOBAL WAVES IN COLD PLASMAS

L. Villard, K. Appert, R. Gruber and J.Vaclavik

Centre de Recherches en Physique des Plasmas
Association EURATOM - Confédération Suisse
Ecole Polytechnique Fédérale de Lausanne
21, Av. des Bains, CH-1007 Lausanne, Switzerland

ABSTRACT

This paper presents numerical methods developed for the calculation of global wave solutions in cold plasmas, in connection with rf heating in the Alfvén and Ion Cyclotron Range of Frequency. Both one-dimensional and two-dimensional geometries are treated, with special emphasis on the toroidal geometry. A scheme based on a variational formulation and the use of finite hybrid elements is presented in detail. The numerical properties of the computational model are carefully examined. It is shown that an approximate solution with good convergence properties in an exact geometry can be obtained.

Table of Contents

1. INTRODUCTION

The study of waves in cold plasmas is one of the oldest subjects of plasma physics [1-3]. In the last few years much effort has been made in this domain [4-10] in great part due to the numerous experimental achievements with using rf waves to heat the plasma [11,12]. Though the properties of such waves in homogeneous plasmas have been well known since a long time, many difficulties arise when the non-uniformity, the finite size and the actual geometry of the plasma in present day experiments, such as tokamaks, are taken into account in the theoretical models.

The first way to tackle the problem has been to treat the differential equations in the WKB approximation, which in multi-dimensional geometries led to the ray-tracing techniques. This approach has given many successful results [13-15]. Unfortunately, it suffers from several limitations. Firstly, the WKB approximation may break down, for example around the resonances. Secondly, in the Alfvén and Ion-Cyclotron Range of Frequency (ICRF), in the actual experimental devices the wavelength is of the same order or larger than the size of the plasma, making a geometrical optics approach inappropriate. Thirdly, in ray-tracing one has to assume single-pass absorption, making the study of eigenmodes impossible.

These reasons, together with the complexity of the analytical methods [16], motivate a different approach to the problem, namely the global determination of the wave field in inhomogeneous, non-uniformly magnetized, finite-size plasmas using numerical techniques to solve

appropriate differential equations. By global solution we mean that:

- the problem is solved in one well-defined geometry, with no matching between different regions having different geometries;
- the solution obtained is the sum of all incident, reflected, transmitted and evanescent waves;
- the differential equations are solved in the whole domain: plasma and vacuum including antenna and shell.

As stated above, it is specially in the Alfvén and ICRF domains that a global solution is needed. We shall therefore limit ourselves to this frequency range.

In this domain, three physical phenomena can be exploited for rf heating:

- the existence of global eigenmodes of the fast magnetosonic wave and of the Alfvén wave [17].

- the perpendicular resonances, either Alfvén or ion-ion hybrid of a multi-ion species plasma (mode conversion regimes).

- the cyclotron damping, assisted by introducing a minority ion species (minority regime).

Our global approach will be able to treat the eigenmodes and the perpendicular resonances in cold plasmas, as well as their simultaneous occurrence.

The numerical methods used to determine the global solution are well-known textbook methods [18,19]. Nevertheless, their application to the study of rf waves in plasmas is rather recent. It is therefore necessary to discuss them in detail, in particular to show clearly their mathematical foundation and to determine where their domain of validity is, in order to develop them to a high degree of credibility. In this paper we shall present the implications of the specific physical and mathematical properties of the problem on the choice of the numerical methods.

The paper is structured as follows. In part 2 we make a few remarks about the one-dimensional problem. The aim of this section is to illustrate some of the basic methods for calculating a global solution. First, we discuss the pertinence of using a cold plasma model for rf heating. We then mention shooting and finite element methods. The treatment of vacuum, including antenna and conducting wall, is also presented. In part 3 we describe the two-dimensional problem. Special care has been taken of the treatment of the toroidal geometry. In particular, we present the recent development of the LION code. LION is based on a variational formulation and finite hybrid elements. The numerical scheme is very carefully examined. By doing convergence studies the accuracy can be measured; comparison with analytical work [20], where possible, as well as with experiment [21] is made; other physical tests, for example of the power balance, are presented. Part 4 discusses the limitations of global wave codes and the possible future improvements of the numerical techniques. We conclude in part 5.

2. GLOBAL WAVE SOLUTION IN ONE-DIMENSIONAL GEOMETRY

2.1 Cold Plasma

The first question which arises is the pertinence of cold plasma model for studying rf heating. In the Alfvén and ion-cyclotron range of frequencies, two phenomena are pure warm plasma effects: the existence of kinetic Alfvén and ion Bernstein waves, and the cyclotron damping. It is therefore necessary to keep in mind that neither 2nd harmonic heating, where the interaction with the ion Bernstein wave is crucial, nor fundamental minority heating, where ion-cyclotron absorption takes place, can ever be described in the context of cold plasma. It then remains the question of the influence of finite temperature on mode conversion scenarios. It has been shown that the cold plasma model is in very good agreement with the warm plasma model, at least in 1-D geometry. When the temperature of the plasma tends to zero, the ion Bernstein wave reduces to the ion-ion perpendicular resonance. But the total power absorbed is exactly the same. In other words, the antenna ignores that the plasma is warm. For more details, see Ref. [22].

2.2 Equations

2.2.1 Basic equations

We consider a cylindrical, non-uniform, current-carrying, multi-species plasma (Fig. 1). All equilibrium quantities depending on r only, we can Fourier-decompose the fields in $\exp\{i(m\theta + kz)\}$. Let us define a local magnetic coordinate system ($\underline{e}_N$, $\underline{e}_\perp$, $\underline{e}_\parallel$) by

$$\underline{e}_N = \underline{\nabla} r / |\underline{\nabla} r|$$
$$\underline{e}_{\parallel} = \underline{B}_0 / B_0 \qquad (2.1)$$
$$\underline{e}_{\perp} = \underline{e}_{\parallel} \times \underline{e}_N$$

and project Maxwell's equations on this system. Moreover, we make the approximation of zero electron mass, leading to $E_{\parallel} = 0$. The most elegant way to write the equations is to use $E_{\perp}$ and $B_{\parallel}$ as variables:

$$A \frac{1}{r} \frac{d}{dr}(rE_{\perp}) = Gk_{\perp}E_{\perp} + (A - k_{\perp}^2)\, i\omega B_{\parallel}$$
$$A \frac{d}{dr}(i\omega B_{\parallel}) = (G^2 - A^2)E_{\perp} - Gk_{\perp}\, i\omega B_{\parallel} \qquad (2.2)$$

with

$$A = \varepsilon_{NN} - k_{\parallel}^2 \quad , \quad \varepsilon_{NN} = \frac{\omega^2}{c^2} S = \frac{\omega^2}{c_A^2} \sum_i \frac{f_i}{1 - (\omega/\omega_{ci})^2}$$
$$G = -i\varepsilon_{N\perp} - \frac{2k_{\parallel} B_{0\theta}}{r B_{0z}} \quad , \quad \varepsilon_{N\perp} = \frac{\omega^2}{c^2} iD = i\frac{\omega^2}{c_A^2} \sum_i \frac{f_i\, \omega/\omega_{ci}}{1 - (\omega/\omega_{ci})^2}$$
$$k_{\parallel} = \left(kB_{0z} + \frac{m}{r} B_{0\theta} \right) / B_0 \qquad (2.3)$$
$$k_{\perp} = \left(\frac{m}{r} B_{0z} - kB_{0\theta} \right) / B_0$$
$$c_A^2 = \frac{B_0^2}{\mu_0 \rho_0}$$

f_i = mass fraction of the i-th ion species = $\dfrac{n_i m_i}{\rho_0}$

(The summations are over all the ion species.)

2.2.2 Singularities

Except for r = 0, the only possible singularities of the equations are given by A = 0. One can easily show that the behaviour of the singular solution around the points $r = r_{res}$, defined by $A(r_{res}) = 0$, is

$$\begin{aligned} E_\perp &\sim \ln|r - r_{res}| \\ B_{//} &\sim \ln|r - r_{res}| \\ B_N &\sim \ln|r - r_{res}| \\ E_N &\sim 1/|r - r_{res}| \\ B_\perp &\sim 1/|r - r_{res}| \end{aligned} \qquad (2.4)$$

The presence of a continuous spectrum, defined by A = 0, and the type of behaviour of the different field components (2.4) will have a consequence on the choice of the numerical method.

A simple way to turn around the singularities is to introduce a small imaginary part ν in A:

$$A \to A + i\nu \qquad (2.5)$$

with $\nu > 0$ to satisfy the causality.

Then the system (2.2) is no longer singular.

Let us make two important remarks:

1° $\omega = \omega_{ci}$ is not a singularity of the equations, despite of the presence of the resonant denominators in ε_{NN} and $\varepsilon_{N\perp}$. Actually, one can show that the circular component of the polarization of the wave field in the ion gyromagnetic direction, $E_+ = E_N + iE_\perp$, satisfies

$$\lim_{\omega \to \omega_{ci}} |E_+| = 0 \quad . \tag{2.6}$$

2° It is crucial that the singular behaviour of $E_\perp$ and $B_\parallel$ is non-analytical (2.4): the power absorption at the singularity is given by

$$\mathrm{Re}\, [\![E_\perp^* B_\parallel]\!]_{r_{res}-0}^{r_{res}+0} \sim -i(i\pi + O(\nu)) \quad . \tag{2.7}$$

This feature allows resonance absorption to occur; the apparent paradox is that we have non-vanishing absorption with damping going to zero. It is then crucial that the numerical techniques guarantee a good description of the singular behaviour.

2.2.3 Antenna and vacuum

We shall neglect the displacement current in all what follows. This is a good approximation for Alfvén wave heating where the vacuum wavelength is much larger than the dimensions of the system. For ICRF in large devices it might be questionable.

Our antenna model is a current sheet located at $r = r_a$ (Fig. 1), with surface currents j_θ and j_z

$$j_\theta = \frac{1}{2}\hat{j}_\theta\, \delta(r-r_a)\, \exp(i(m\theta + kz - \omega t)) + c.c.,$$
$$j_z = \frac{1}{2}\hat{j}_z\, \delta(r-r_a)\, \exp(i(m\theta + kz - \omega t)) + c.c. \qquad (2.8)$$

In the region between antenna and shell, feeder currents j_r and $j_\perp$ are introduced to satisfy div $\underline{j} = 0$.

The surface currents can be treated as a discontinuity of the wave magnetic field, while the feeder currents are volume currents which have to be included in the vacuum wave equations. These can be brought to the form

$$\frac{d}{dr}\begin{pmatrix} rB_N \\ B_{//} \end{pmatrix} + \begin{bmatrix} 0 & i\,\frac{(k_\perp^2 + k_{//}^2)\,r}{k_{//}} \\ -i\,\frac{k_{//}}{r} & \frac{2B_{0\theta}k_\perp}{rB_{0z}k_{//}} \end{bmatrix} \begin{pmatrix} rB_N \\ B_{//} \end{pmatrix}$$
$$= \begin{pmatrix} \frac{k_\perp}{k_{//}}\, r j_r \\ -\frac{2iB_{0\theta}}{rB_{0z}k_{//}}\, j_r - j_\perp \end{pmatrix} . \qquad (2.9)$$

2.2.4 Regularity, boundary and matching conditions

1° On the axis, the equations have the usual singularity of the cylindrical geometry. But for physical reasons, the solution has to be regular. Writing $E_\perp$ and $B_\parallel$ as

$$E_\perp = r^{|m|-1}\,\hat{E}$$

$$B_\parallel = \frac{1}{i\omega}\, r^{|m|}\,\hat{B} \qquad (2.10)$$

and expanding around r = 0: $\hat{E} = e_0+e_1 r+\ldots$, $\hat{B} = b_0+b_1 r+\ldots$, $A = a_0+a_1 r+\ldots$, $G = g_0+g_1 r+\ldots$, we use the equation (2.2) to obtain in lowest order in r

$$\begin{bmatrix} a_0|m| - m g_0 & m^2 \\ a_0^2 - g_0^2 & a_0|m| + m g_0 \end{bmatrix} \begin{bmatrix} e_0 \\ b_0 \end{bmatrix} = 0. \qquad (2.11)$$

The regularity condition is then

$$\hat{E}(r=0) = \frac{m^2}{m g_0 - |m| a_0}\,\hat{B}(r=0) \qquad (2.12)$$

2° At the plasma-vacuum interface, we require the fields be continuous. We only have to transform $E_\perp$ to B_N

$$B_N (r = r_p) = - \frac{k_{//}}{\omega} E_\perp (r = r_p) \quad . \tag{2.13}$$

3° At the antenna, the surface currents (2.8) impose

$$[\![B_N]\!] = 0 \quad , \quad [\![B_{//}]\!] = - \hat{j}_\theta + \frac{B_{0\theta}}{B_{0z}} \hat{j}_z \quad , \tag{2.14}$$

where the double bracket indicates a jump across the antenna from the inside to the outside.

4° On the shell, the infinite conductivity imposes

$$B_N (r = r_s) = 0 \quad . \tag{2.15}$$

The equations (2.2) and (2.9), with (2.12)-(2.15), determine a unique solution.

2.2.5 Power

The total complex power delivered by the antenna is

$$P_a = \frac{1}{2} \int_V \underline{j} \cdot \underline{E}^* \, dV \quad , \tag{2.16}$$

where V is the vacuum domain.

It can be compared to the total power transmitted through the plasma-vacuum interface

$$P_P = \frac{1}{2}\int_{\partial\Omega} E_\perp^* B_{//}\, d\sigma \quad . \tag{2.17}$$

2.3 Shooting Methods

The simplest numerical scheme is to solve (2.2), (2.9), (2.12) - 2.15) as an initial value problem with a Runge-Kutta algorithm. The principle is to determine the fundamentals of the system of equations and to use the matching conditions to fix the constants of integration. The presence of singularities forces us to introduce $\nu \neq 0$ in the equations (see 2.5) and to have an adjustable step in order to control the accuracy. We proceed as follows:

1° We start at $r = \delta <<< 1$ with a given initial value, using the regularity condition (2.12). We integrate the plasma equations (2.2) up to the plasma-vacuum interface $r = r_p$.

2° We use (2.13) to transform $E_\perp$ to B_N, and integrate the vacuum equations (2.9) with $j_r = j_\perp = 0$ up to the antenna $r = r_a$. We have then the solution at $r_a - 0$

$$C_1 \begin{pmatrix} \mathcal{B}_N^{(A)} \\ \mathcal{B}_{//}^{(A)} \end{pmatrix} \quad . \tag{2.18}$$

3° In the region between the antenna and shell we integrate once the homogeneous (H) equations, i.e. (2.9) with $j_N = j_\perp = 0$, and once the inhomogeneous ones (N) starting with the condition (2.15). We have the solution at $r_a + 0$

$$C_2 \begin{pmatrix} \mathcal{B}_N^{(H)} \\ \mathcal{B}_{//}^{(H)} \end{pmatrix} + \begin{pmatrix} \mathcal{B}_N^{(N)} \\ \mathcal{B}_{//}^{(N)} \end{pmatrix} \tag{2.19}$$

4° The matching conditions at the antenna (2.14) introduced into (2.18) and (2.19) yield the integration constants

$$\begin{aligned} C_1 &= \frac{1}{\mathcal{B}_N^{(A)}} \left(C_2 \mathcal{B}_N^{(H)} + \mathcal{B}_N^{(N)} \right) \\ C_2 &= \frac{1}{\mathcal{D}} \left(-\mathcal{B}_{//}^{(N)} + \frac{\mathcal{B}_{//}^{(A)} \mathcal{B}_N^{(N)}}{\mathcal{B}_N^{(A)}} \right) - \hat{j}_\theta + \frac{\mathcal{B}_{0\theta}}{\mathcal{B}_{0z}} \hat{j}_z \\ \mathcal{D} &= \mathcal{B}_{//}^{(H)} - \frac{\mathcal{B}_{//}^{(A)} \mathcal{B}_N^{(H)}}{\mathcal{B}_N^{(A)}} \end{aligned} \tag{2.20}$$

5° We use (2.16) and (2.17) to calculate the total power.

The real antenna excitation structure can be Fourier-decomposed in $\exp\{i(m\Theta + kz - \omega t)\}$. The whole procedure (1°) to (5°) is repeated for each Fourier component. The total power is simply the sum of the powers of all components.

An example of application of such a method has been the calculation of antenna coupling for Alfvén wave heating in TCA [23]. Different configurations of antennae were used: variation of its excitation spectrum, tilt, positioning the feeders, etc., in order to optimize the coupling and the radial absorption profile. Global modes can also be found using this method; in this case the power varies as $1/\nu$, while if there is a resonant layer in the plasma the power is independent of ν for sufficiently small ν. If the antenna excites neither a resonant layer nor a global mode the power is proportional to ν.

2.4 Finite Element Method

The principle of this method [18,19] can be summarized as follows:

1° We discretize the domain on a general non-uniform mesh $\{r_i\}^N$.

2° We expand the unknown fields E in a set of basis functions Γ_j, $j = i,\ldots, N$:

$$\underline{E}(r) = \sum_{j=1}^{N} x_j \underline{\Gamma}_j(r) \quad . \tag{2.21}$$

The Γ_j are polynomials having a finite support (see Fig. 2).

3° We introduce (2.21) in the differential equations to obtain an algebraic system of equations for the x_j. This is usually done by multiplying the equations by sufficiently regular test functions and integrating by parts. On using the basis functions as test functions we get the algebraic problem

$$\underline{\underline{A}}\ \underline{x} = \underline{b} \tag{2.22}$$

where $\underline{b}$ is the source term due to the antenna. The matrix $\underline{\underline{A}}$ is the discretized version of the operator defined by the differential equations; in our case it is a complex non-hermitian band matrix. Its bandwidth depends on the number of unknown field components and on the order of the basis functions.

The choice of the basis functions is in principle free. Our problem, however, presents a particularity: the existence of a continuous spectrum ($A = 0$, see (2.3)) requires that the basis functions reproduce locally the different singular behaviours of the different field components (2.4). Otherwise spectral pollution occurs, which means that the discretized continuum exhibits spurious modes which can be completely outside the exact range, and sometimes even spread among physical global modes. An example is given in Fig. 3 (right-hand side) for the case of ideal MHD ($\omega/\omega_{ci} = 0$), using regular finite elements of first order [24]. These unphysical modes can be eliminated by increasing the number of intervals, but it can be an unrewarding task to make such convergence studies for each case. In the case of the

cylindrical cold plasma, we were able to use $E_\perp$ and $B_\parallel$ as variables by eliminating E_N. Since they have the same singular behaviour (2.4), there is no problem in using regular finite elements.

However, we shall see that it is no longer possible in toroidal geometry; one is forced to use E_N and $E_\perp$ as variables which have different singular behaviour (2.4). This suggests the use of different basis functions for E_N and $E_\perp$, e.g. piecewise constant for E_N and piecewise linear for $E_\perp$, such that $dE_\perp/dr$ has the same behaviour as E_N. This technique was successfully tested in the frame of ideal MHD [24]; spectral pollution disappears (Fig. 3, second spectrum from the right).

Another technique is the use of hybrid elements [25]. It consists in considering a function and its derivative as independent variables. This technique will be presented more in detail in the next chapter.

Brief discussion

The advantage of the shooting method over finite elements is its simplicity. A problem arises, however, if there exists an evanescent wave branch: when integrating backwards, the solution will explode exponentially due to the numerical noise. Fortunately, in a cold plasma the wave is not too strongly evanescent, so that one can still guarantee a reasonable accuracy if the evanescent region is not too large. For a warm plasma, the presence of an evanescent Bernstein wave prevents completely the use of shooting methods.

On the other hand, the finite element method solves the problem as a boundary value problem; unphysical exponentially growing solutions cannot appear. This is the great advantage of this method.

3. GLOBAL WAVE SOLUTION IN TWO-DIMENSIONAL (TOROIDAL) GEOMETRY

3.1 Introduction

The two first successful attempts to determine a global solution of the wave equations in the ICRF in toroidal geometry were made by Itoh et al. [6,26] and Colestock et al. [27]. Both numerical methods were finite difference schemes. The first authors used a simplified geometry via expansion in inverse aspect ratio. The configuration was a cylindrical plasma with a circular cross-section, a density depending on the minor radius and an axial magnetic field depending on the major radius. On the other hand, the first global wave code in real toroidal geometry, but restricted to the study of Alfvén wave heating in ideal MHD ($\omega/\omega_{ci} = 0$), was constructed a few years ago [28,9]; its development was based on the ERATO stability code [29].

In this section we present the first global wave code which solves the wave equations relevant for both Alfvén wave and ICRF heating in a cold toroidal plasma, with no geometrical approximation. The problem is formulated variationally and solved using finite hybrid elements.

3.2 Toroidal Geometry

The axisymmetric equilibrium magnetic field can be written

$$\underline{B}_o = T(\psi)\,\underline{\nabla}\phi \;+\; \underline{\nabla}\phi \times \underline{\nabla}\psi \qquad (3.1)$$

where ψ = const defines a magnetic surface and ϕ is the toroidal angle (Fig. 4).

The toroidal and poloidal components, $B_{ot} = T/r$ and $B_{op} = |\underline{\nabla}\psi|/r$, have a two-dimensional functional dependence. This implies that the magnitude of the magnetic field varies along a field line. As a consequence, it is impossible to define the parallel wavelength in the same way as in the cylinder by an algebraic expression (2.3); $k_\parallel$ is now not only a function of position but it is a differential operator:

$$ik_\parallel = \nabla_\parallel = \frac{1}{B_o}\,\underline{B}_o \cdot \underline{\nabla} \qquad (3.2)$$

This means that the relation giving the Alfvén and ion-ion hybrid perpendicular resonances ($\varepsilon_{NN} - k_\parallel^2 = 0$ in 1-D) - hence the resonance absorption - is also a differential operator. This complication makes analytical work difficult. Studies by Hellsten & al. [7] indicated that the resonant surfaces lie on the magnetic surfaces (ψ = const). Our global code will be able to check this result as well as it will show how the usual one-dimensional picture is recovered when the size of the plasma is increased, or when the poloidal field is decreased [30].

We shall see in the next section that the magnetic surfaces (ψ = const) have an interesting property for the partial differential system of equations.

3.3 Equations

3.3.1 Basic equations

We consider a plasma in an axisymmetric equilibrium. The magnetic field is given by (3.1) and the density profile ρ_o, as well as the concentrations of the different ions species f_j, can be arbitrarily specified. In our case we have chosen ρ_o and f_j to depend on ψ only. We write Maxwell's equation in the local magnetic coordinate system ($\underline{e}_N$, $\underline{e}_\perp$, $\underline{e}_\parallel$) defined by $\underline{e}_N = \underline{\nabla}\psi / |\underline{\nabla}\psi|$, $\underline{e}_\parallel = \underline{B}_o/B_o$, $\underline{e}_\perp = \underline{e}_\parallel \times \underline{e}_N$

$$\underline{\underline{rot}}\ \underline{\underline{rot}}\ \underline{E} - \underline{\underline{\varepsilon}}\ \underline{E} = 0 \quad , \tag{3.3}$$

where $\underline{\underline{\varepsilon}}$ is the dielectric tensor of a cold current-carrying multi-species plasma. It is a differential operator. It neglects any finite β effects, such as finite Larmor radius and equilibrium pressure, but it takes into account the equilibrium plasma current density $\underline{j}_o$. Finite electron mass has been neglected, leading to $E_\parallel = 0$. We have then

$$\underline{\underline{\varepsilon}} = \begin{pmatrix} \varepsilon_{NN} & \varepsilon_{N\perp} \\ -\varepsilon_{N\perp} & \varepsilon_{NN} \end{pmatrix} + \frac{\underline{j}_o \cdot \underline{B}_o}{B_o^2} \begin{pmatrix} rot_N\, \underline{e}_N & rot_N\, \underline{e}_\perp \\ rot_\perp\, \underline{e}_N & rot_\perp\, \underline{e}_\perp \end{pmatrix} , \tag{3.4}$$

where

$$\varepsilon_{NN} = \frac{\omega^2}{c^2} S = \frac{\omega^2}{c_A^2} \sum_i \frac{f_i}{1-(\omega/\omega_{ci})^2}$$

$$\varepsilon_{N\perp} = \frac{\omega^2}{c^2} iD = i\frac{\omega^2}{c_A^2} \sum_i \frac{f_i\, \omega/\omega_{ci}}{1-(\omega/\omega_{ci})^2} \qquad \text{(idem in 2.3)} \qquad (3.5)$$

Notice that the operators rot_N and $\mathrm{rot}_\perp$ act also on $\underline{E}$.

The reason why we included the equilibrium current in the dielectric tensor is that this term has been shown to be important for Alfvén wave heating in cylindrical geometry, e.g. the existence of global eigenmodes of the Alfvén wave [17], or the effect of assisting to deposit energy in the central resonant layers [31]. Whether this term is important also in the ICRF is not yet clear.

3.3.2 Variational form of the equations

It can be obtained by operating on eq. (3.3) with:

$$\int_\Omega dV\, \underline{\tilde{E}} \cdot \qquad , \qquad \Omega = \text{plasma volume}, \qquad (3.6)$$

where $\underline{\tilde{E}}$ is a sufficiently regular test function. After partial integration, we have

$$\int_{\Omega} dV \left(\underline{rot}\, \underline{\tilde{E}} \cdot \underline{rot}\, \underline{E} - \frac{\underline{j_0} \cdot \underline{B_0}}{B_0^2}\, \underline{\tilde{E}} \cdot \underline{rot}\, \underline{E} - \underline{\tilde{E}} \cdot \begin{bmatrix} \varepsilon_{NN} & \varepsilon_{N\perp} \\ -\varepsilon_{N\perp} & \varepsilon_{NN} \end{bmatrix} \underline{E} \right)$$

$$- i\omega \int_{\partial\Omega} \underline{d\sigma} \cdot (\underline{\tilde{E}} \times \underline{B}) = 0. \qquad (3.7)$$

3.3.3 Singularities and symmetries

The operator in (3.7) is non-compact due to the presence of singularities. As discussed in section 3.2, they are described by a differential equation. A simple way to treat the problem is to make the transformation

$$\varepsilon_{NN} \rightarrow \varepsilon_{NN} + 2i\nu\omega^2\rho_0 \qquad (3.8)$$

with $\nu > 0$ to satisfy the causality. We have chosen ν = const. One could also take the collisional form of ε_{NN} or replace ω by $\omega + i\nu$ [6]. But these options have the disadvantage that the imaginary part of ε_{NN} peaks around $\omega = \omega_{ci}$, with a width proportional to ν. Since ν has to be sufficiently large to turn around the discretized singularities, it would introduce pseudo-cyclotron absorption acting on the total electric field $\underline{E}$ and not only on the polarization E_+ [30].

With $\nu \neq 0$ the operator in (3.7) has no longer singularities, but it has lost its hermiticity.

The axisymmetry of the equilibrium allows us to decompose the wave field $\underline{E}$ and the test function $\underline{\tilde{E}}$ in Fourier series in the toroidal angle

$$\underline{E} = \sum_n \underline{E}_n e^{in\phi}$$
$$\underline{\tilde{E}} = \sum_{n'} \underline{\tilde{E}}_{n'} e^{in'\phi} \quad . \tag{3.9}$$

Introducing these expressions in the variational form (3.7) and integrating over ϕ, we can treat each Fourier component separately since for a given n only the term n' = -n will contribute. We then have

$$\frac{\partial}{\partial\phi} = in \quad \text{when acting on } \underline{E} \ ,$$
$$\frac{\partial}{\partial\phi} = -in \quad \text{when acting on } \underline{\tilde{E}} \ . \tag{3.9b}$$

The operator in (3.7) is not symmetric with respect to the "up-down" transformation (Fig. 5)

$$\underline{B}_0 \rightarrow -\underline{B}_0$$
$$\underline{j}_0 \rightarrow -\underline{j}_0 \quad . \tag{3.10}$$

This is due to the privileged direction of the ion gyromagnetic rotation. As a consequence, we have to solve the equations not only in a half-plane like in ideal MHD, but in the whole poloidal plane.

The finite aspect ratio breaks the cylindrical symmetry. The azimuthal wavenumbers m cease to be good "quantum" numbers. They are no longer independent: toroidal coupling occurs between modes of a given m and m ± 1,... . The ellipticity of the cross-section couples m to m ± 2,... . These effects have been studied in the context of ideal MHD [9]. When a line $\omega = \omega_{ci}$ crosses the plasma, one expects the break of cylindrical symmetry to be even larger, due to the vertical ω_{ci} structure.

Let us make the following remark: each break of symmetry corresponds to a splitting of degenerated modes, thus allowing for many of them to exist and to be possibly excited by the antenna. The less the system is symmetric, the more one can expect the mode structure to be complex.

3.3.4 Toroidal coordinates

We have chosen ψ, χ, ϕ as coordinates (see Fig. 4).

1° The relation $\psi =$ const defines the magnetic surfaces (eq. 3.1). For convenience we shall use the "radial" variable s:

$$s = \sqrt{\frac{\psi}{\psi_s}} \tag{3.11}$$

where ψ_s is the value of ψ at the surface of the plasma.

2° The "poloidal angle" χ is such that the Jacobian defined by

$$\mathcal{J} = \left[\underline{\nabla}\psi \cdot (\underline{\nabla}\chi \times \underline{\nabla}\phi) \right]^{-1} \tag{3.12}$$

becomes

$$\mathcal{J} = \frac{qr^2}{T} \quad , \tag{3.13}$$

where $T = T(\psi)$ is defined in (3.1) and $q = q(\psi)$ is the safety factor

$$q(\psi) = \frac{1}{2\pi} \oint \frac{1}{r} \frac{B_{ot}}{B_{op}} \, dl \tag{3.14}$$

where dl is a length element in the poloidal plane on a ψ = const surface. We have

$$dl = \mathcal{J} B_{op} \, d\chi \tag{3.15}$$

Notice that r^2/J is a function of ψ only.

3° The choice of the toroidal angle ϕ is natural since we have decomposed the wave field in Fourier series in ϕ (3.9).

Instead of E_N and $E_\perp$, we shall use the variables V and X defined by

$$\underline{E} = \frac{VT}{2\psi_s s} \underline{\nabla}\psi - XT \underline{\nabla}\chi + \frac{Xr^2}{\mathcal{J}} \underline{\nabla}\phi \, . \tag{3.16}$$

Thus

$$E_N = \frac{T\,|\underline{\nabla}\psi|}{2\psi_s s}\,(V-\beta_\chi X) \qquad (3.16b)$$

$$E_\perp = -\frac{r^2 B_o}{J\,|\underline{\nabla}\psi|}\,X \quad ,$$

where β_χ is the non-orthogonality:

$$\beta_\chi = \frac{2\psi_s s}{|\underline{\nabla}\psi|^2}\,\underline{\nabla}\psi\cdot\underline{\nabla}\chi \quad . \qquad (3.16c)$$

Using the relations

$$\underline{\nabla} = \underline{\nabla}\psi\frac{\partial}{\partial\psi} + \underline{\nabla}\chi\frac{\partial}{\partial\chi} + \underline{\nabla}\phi\frac{\partial}{\partial\phi}$$

$$\underline{B}_o\cdot\underline{\nabla} = \frac{1}{J}\left(\frac{\partial}{\partial\chi} + q\frac{\partial}{\partial\phi}\right) \qquad (3.17)$$

$$\frac{\partial}{\partial\psi} = \frac{1}{2\psi_s s}\frac{\partial}{\partial s}$$

$$dV = 2J\psi_s s\,ds\,d\chi \quad ,$$

one can write

$$\underline{rot}\,\underline{E} = \left(\underline{\nabla}\frac{VT}{2\psi_s s}\right)\times\underline{\nabla}\psi - (\underline{\nabla}\chi T)\times\underline{\nabla}\chi + \left(\underline{\nabla}\frac{\chi r^2}{J}\right)\times\underline{\nabla}\phi$$

$$= A_1\frac{\underline{\nabla}\psi}{|\underline{\nabla}\psi|} + A_2\frac{\underline{\nabla}\phi}{|\underline{\nabla}\phi|} + A_3\frac{\underline{\nabla}\phi\times\underline{\nabla}\psi}{|\underline{\nabla}\phi|\,|\underline{\nabla}\psi|} \quad ,$$

$$A_1 = \frac{r^2}{J^2|\underline{\nabla}\psi|}\left(\frac{\partial}{\partial\chi} + inq\right)X \qquad (3.18)$$

$$A_2 = \frac{-B_{ot}\,r^2}{2\psi_s s\,J}\left(\frac{\partial X}{\partial s} + \frac{\partial V}{\partial\chi} + \left(\frac{\partial}{\partial s}\ln T\right)X\right)$$

$$A_3 = \frac{B_{op}\,r^2}{2\psi_s s\,J}\left(inq\,(V-\beta_\chi X) - \frac{\partial X}{\partial s} - \beta_\chi\frac{\partial X}{\partial\chi} - \left(\frac{\partial}{\partial s}\ln\frac{r^2}{J}\right)X\right)$$

The same expression holds for $\underline{\mathrm{rot}}\ \underline{\tilde{E}}$, except that n has to be replaced by -n (see (3.9b)).

With the relations (3.16) - (3.18), the variational form (3.7) can be written as

$$\int_0^1 ds \int_0^{2\pi} d\chi \left(\sum_{j=1}^{8} c_j I_j^* \gamma_j \right) + S = 0 \quad , \tag{3.19}$$

where

$$\begin{aligned}
I_1 &= \gamma_1 = X \\
I_2 &= \gamma_2 = V - \beta_\chi X \\
I_3 &= X \quad , \quad \gamma_3 = V \\
I_4 &= V \quad , \quad \gamma_4 = X \\
I_5 &= \gamma_5 = \frac{\partial X}{\partial \chi} + inq X \\
I_6 &= \gamma_6 = \frac{\partial X}{\partial s} + \frac{\partial V}{\partial \chi} \\
I_7 &= \gamma_7 = \frac{\partial X}{\partial s} + \beta_\chi \frac{\partial X}{\partial \chi} + \beta_\chi inq X + HX - inq V \\
I_8 &= \gamma_8 = X \quad ,
\end{aligned} \tag{3.19b}$$

$$c_1 = \frac{-2\psi_s s r^2}{B_{op}^2 \eta}\ \hat{\varepsilon}$$

$$c_2 = \frac{-\eta B_{op}^2 B_{ot}^2 r^4}{2\psi_s s B_o^2}\ \hat{\varepsilon}$$

$$c_3 = \frac{-B_{ot} r^3}{B_o}\ i\hat{q}$$

$$c_4 = -c_3$$

$$c_5 = \frac{2\psi_s s r^2}{B_{op}^2 \eta^3} \qquad (3.19c)$$

$$c_6 = \frac{B_{ot}^2 r^4}{2\psi_s s \eta}$$

$$c_7 = \frac{B_{op}^2 r^4}{2\psi_s s \eta}$$

$$c_8 = \frac{-2 r^4 q_o K}{\eta s} \quad ,$$

$$\hat{\varepsilon} = \rho_o \omega^2 \sum_k \frac{f_k}{1-(\omega/\omega_{ck})^2}$$

$$\hat{q} = \rho_o \omega^2 \sum_k \frac{f_k \omega/\omega_{ck}}{1-(\omega/\omega_{ck})^2} \qquad (3.19d)$$

$$H = \frac{\partial}{\partial s} \ln \frac{r^2}{\eta} + \frac{2\psi_s s}{r B_{op}^2} j_{o\phi}$$

$$K = \frac{2\psi}{q_o} \left(\frac{j_{o\phi}^2}{r^2 B_{op}^2} + \frac{j_{o\phi}}{2r} \frac{\partial}{\partial \psi} \ln r^2 B_{op}^2 \right)$$

$$j_{o\phi} = \underline{j}_o \cdot \underline{\nabla}\phi \ / \ |\underline{\nabla}\phi| \quad ,$$

$$S = -i\omega \int_{\partial\Omega} d\underline{\sigma} \cdot (\tilde{\underline{E}} \times \underline{B}) \qquad (3.19e)$$

This section may appear unnecessarily complicated to the reader who is unfamiliar with toroidal geometry. For example, one may think that it is much simpler for the algebra to take r,z,ϕ as coordinates. In this case both variables have derivatives with respect to r and z, making the differential system appear as a fourth order system. The great advantage of using magnetic coordinates is that one variable, V, has no derivative in the ψ direction, thus lowering the order of the differential operator. This has many advantages for the numerical resolution. Moreover, we have the same differential structure as for the ideal MHD stability problem. It is then natural to take advantage of the existence of the numerical code ERATO [29] by using the same coordinate system.

3.3.5 Regularity, boundary and matching conditions. Vacuum solution

The regularity on the magnetic axis (s = 0) imposes the fields to remain finite. Since $\lim_{s\to 0} |\underline{\nabla}\psi| = 0$ and $\lim_{s\to 0} |\underline{\nabla}\psi|/s = \text{const}$, from (3.16) we conclude

$$\lim_{s\to 0} \chi = 0 \quad . \qquad (3.20)$$

The surface term S in (3.19) has to be connected to the vacuum solution via boundary conditions. Here we require the fields be continuous across the plasma-vacuum interface.

Our model of antenna is a current-carrying sheet surrounding the plasma (Fig. 6). As in the 1-D case, we shall neglect the displacement current. The antenna surface is defined by

$$\mathcal{D}(\underline{r}) = 0 \tag{3.21}$$

and its current $\underline{j}_a$, satisfying automatically $\underline{\nabla} \cdot \underline{j}_a = 0$, is

$$\underline{j}_a = \delta(\mathcal{D})\, \underline{\nabla}\mathcal{D} \times \underline{\nabla}\beta \quad \exp(i(n\phi - \omega t)) \quad , \tag{3.22}$$

where β is the "current potential". For the sake of simplicity we assume β to be a function of θ only. Then β determines the current in the poloidal direction, and $d\beta/d\theta$ is related to the current in the toroidal direction [9].

The matching conditions at the antenna are

$$\begin{aligned} \underline{n}_a \times [\![\underline{B}]\!] &= \underline{n}_a \times \underline{\nabla}\beta \\ \underline{n}_a \cdot [\![\underline{B}]\!] &= 0 \quad , \end{aligned} \tag{3.23}$$

where $\underline{n}_a$ is the outer normal to the antenna; the double bracket indicates a jump across the antenna from the inside to the outside.

The vacuum region is surrounded by a perfectly conducting shell where we have

$$\underline{n}_s \cdot \underline{B} = 0 \quad , \tag{3.24}$$

where $\underline{n}_s$ is the outer normal to the shell.

The vacuum equations are

$$\underline{\mathcal{B}} = \underline{\nabla}\,\Phi$$
$$\nabla^2\Phi = 0 \qquad (3.25)$$

We are now ready to express the surface term S (3.19e) in terms of the vacuum solution. S can be written, using $E_\parallel = 0$ in the plasma, as

$$S = -i\omega \int_{\partial\Omega} \tilde{E}_\perp \mathcal{B}_\parallel \, d\sigma \qquad (3.26)$$

Using the vacuum equations (3.25) and the identity

$$\mathrm{rot}_N(\Phi \underline{\tilde{E}}) = i\omega \Phi \tilde{\mathcal{B}}_N + \tilde{E}_\perp \mathcal{B}_\parallel \quad , \qquad (3.27)$$

we have

$$S = \omega^2 \int_{\partial\Omega} \Phi \tilde{\mathcal{B}}_N \, d\sigma \qquad (3.28)$$

or, with $i\omega B_N = -\nabla_\parallel E_\perp$,

$$S = i\omega \int_{\partial\Omega} \Phi \nabla_\parallel \tilde{E}_\perp \, d\sigma \qquad (3.29)$$

The potential Φ is functionally related to its normal derivative on the boundaries of the vacuum region (the plasma boundary, antenna

and shell) via Green's theorem. Using the boundary and matching conditions (3.23) and (3.24) one can write Φ on the plasma boundary as

$$\Phi(\underline{r}) = \int_{\partial\Omega} Q(\underline{r},\underline{r}')\, \underline{\nabla}\Phi(\underline{r}')\cdot \underline{d\sigma}' \;+\; \Phi_E(\underline{r}) \quad , \tag{3.30}$$

where Φ_E is the source term due to the antenna. The derivation of the full expressions for Q and Φ_E has been given in Ref. [9].

Introducing (3.30) in (3.29), we obtain

$$S = -\int_{\partial\Omega}\int_{\partial\Omega} Q(\underline{r},\underline{r}') \left(\nabla_{\!/\!/}\, \tilde{E}_{\perp}(\underline{r}')\right)\left(\nabla_{\!/\!/}\, E_{\perp}(\underline{r})\right) d\sigma\, d\sigma'$$

$$+\, i\omega \int_{\partial\Omega} \Phi_E(\underline{r}') \left(\nabla_{\!/\!/}\, \tilde{E}_{\perp}(\underline{r}')\right) d\sigma' \quad , \tag{3.31}$$

with

$$Q = M_{pp}^{-1}\left[\, E_{pp} - (D_{ps} - 2I)\, D_{ss}^{-1}\, E_{sp}\,\right]$$

$$\Phi_E = M_{pp}^{-1}\left[\, (D_{ps} - 2I)\, D_{ss}^{-1} D_{sa} + 2I - D_{pa}\,\right]\beta$$

$$M_{pp} = D_{pp} - 2I - (D_{ps} - 2I)\, D_{ss}^{-1} D_{sp}$$

$$D_{\mu\nu} f(\underline{r}) = \frac{1}{2\pi} \int_{\nu} \left(f(\underline{r}') - f(\underline{r})\right) \underline{\nabla}' G(\underline{r}_{\mu}, \underline{r}_{\nu}')\cdot \underline{d\sigma}'$$

$$E_{\mu\nu} f(\underline{r}) = \frac{1}{2\pi} \int_{\nu} G(\underline{r}_{\mu}, \underline{r}_{\nu}')\, \underline{\nabla}' f(\underline{r}')\cdot \underline{d\sigma}' \tag{3.31b}$$

$$G(\underline{r}_{\mu}, \underline{r}_{\nu}) = 1 \,/\, |\underline{r}_{\mu} - \underline{r}_{\nu}|$$

μ, ν = p (plasma), a (antenna) or s (shell).

An alternative to the Green's function technique is the numerical integration of vacuum equations, e.g. using finite elements [32].

Once the antenna current (3.22) is specified, the solution of the variational form (3.19), with its vacuum contribution (3.31) and the regularity condition (3.20), is uniquely determined. Before explaining the numerical construction of this solution, we shall derive a few expressions which are interesting from the physical point of view.

3.3.6 Power, Poynting flux and power balance

The total power delivered by the antenna is

$$P_a = \frac{1}{2}\int_V dV\, \underline{j}_a \cdot \underline{E}^* \quad , \qquad V = \text{vacuum region} \quad . \tag{3.32}$$

It can be written, using the definition of the antenna current (3.22), after partial integration and use of Maxwell's equations as

$$P_a = -\frac{i\omega}{2}\int_a \beta\, \underline{B}^* \cdot d\underline{\sigma}_a \tag{3.33}$$

The integral is a surface integral along the antenna. With the same Green's function technique as described above, $\underline{B}^* \cdot d\underline{\sigma}_a$ can be expressed as a surface integral along the plasma-vacuum interface

$$\underline{B}^* \cdot d\underline{\sigma}_a = \int_p Z(\underline{r}_a, \underline{r}_p)\left(\nabla_{//} E_{\perp}^*(\underline{r}_p)\right) d\sigma_p + \Psi_E(\underline{r}_a) \quad , \tag{3.34}$$

and

$$P_a = -\frac{i\omega}{2}\left(\int_a \beta(\underline{r}_a) \int_p Z(\underline{r}_a, \underline{r}_p)\left(\nabla_{//} E_{\perp}^*(\underline{r}_p)\right) d\sigma_p d\sigma_a + \int_a \beta(\underline{r}_a)\Psi_E(\underline{r}_a) d\sigma_a \right) \quad , \tag{3.35}$$

with

$$Z = T_{pa}^{-1}\left(V_{pp} - U_{pp} Q\right)$$

$$\beta\Psi_E = T_{pa}^{-1} U_{pp} \Phi_E$$

$$T_{pa} = E_{pa} - (D_{pa} - 2I) D_{aa}^{-1} E_{aa} \tag{3.35b}$$

$$U_{pp} = D_{pp} - 2I - (D_{pa} - 2I) D_{aa}^{-1} D_{ap}$$

$$V_{pp} = E_{pp} - (D_{pa} - 2I) D_{aa}^{-1} E_{ap} \quad .$$

Another interesting quantity is the total power transmitted through the plasma surface

$$P_p = \frac{1}{2}\int_{\partial\Omega} (\underline{E}^* \times \underline{B}) \cdot d\underline{\sigma}_p \quad . \tag{3.36}$$

It can be evaluated either from the explicit calculation of the Poynting vector $\underline{S}$, or directly from the variational form (see 3.7).

The global power balance is

$$Re\ P_a = Re\ P_p \quad . \tag{3.37}$$

The local power absorption density $\mathrm{div}\frac{1}{2}\mathrm{Re}(\underline{E}^* \times \underline{B})$ can be written as

$$P_d(\underline{r}) = \frac{1}{2\omega}\left(Im\,\varepsilon_{NN}\,|E_+|^2 + \right.$$
$$\left. + 2\,Im\,(\varepsilon_{NN} + i\varepsilon_{N\perp})\,Im\,(E_N^* E_\perp)\right) . \tag{3.38}$$

In our case we have an imaginary part only in ε_{NN} (see 3.8); thus this relation reduces to

$$P_d(\underline{r}) = \frac{1}{2\omega}\,Im\,\varepsilon_{NN}\,|\underline{E}|^2 \tag{3.39}$$

To check the validity of the solution, we compare the power absorbed in a given volume with the Poynting flux across the surface of this volume. Let Ω_ψ be a torus defined by a ψ = const surface, and let us define the Poynting flux P_S as

$$P_s(\psi) = \frac{1}{2}\int_{\partial\Omega_\psi} Re\,(\underline{E}^* \times \underline{B})\cdot d\underline{\sigma}_\psi \tag{3.40}$$

and the power flux P_e as

$$P_e(\psi) = \int_{\Omega_\psi} P_d(\underline{r})\, dV \quad . \tag{3.41}$$

The local power balance is evidently

$$P_s(\psi) = P_e(\psi) \quad , \forall \psi \quad . \tag{3.42}$$

One can also compare $\dfrac{dP_s}{d\psi}$ with $\int_{\partial\Omega_\psi} P_d(\underline{r})\, d\sigma_\psi$. (3.42b)

Finally, we must have

$$Re\, P_a = Re\, P_p = P_s(\psi_s) = P_e(\psi_s) \tag{3.43}$$

where ψ_s is the magnetic flux at the plasma-vacuum interface. The Poynting vector $\underline{S} = \underline{E}^* \times \underline{B}$ can be evaluated using $\underline{B} = 1/i\omega\ \underline{\mathrm{rot}E}$ and the expression (3.18) for $\underline{\mathrm{rot}E}$.

3.4 Numerical Solution of the Variational Form

We now have all the material necessary to describe the numerical scheme used in the LION code. It consists of five distinct parts.

3.4.1 Equilibrium

The equilibrium can be computed either in a separate code or by using the Solovev analytical model [33]. In both cases one obtains the values of ψ, solution of the Grad-Shafranov equation, on a rectangular mesh in (r,z): $\{\psi_{ij} = \psi(r_i,z_j),\ i = 1..N_r,\ j = 1..N_z\}$. In the actual version of the code the equilibrium is assumed to be symmetric in z and is determined only in the upper half-plane. The plasma domain is covered with a rectangular non-uniform mesh in (s,χ): $\{(s_i,\chi_j),\ i = 1..N_\psi,\ j = 1..N_{pol}\}$ (s is defined in eq. 3.11). The information has to be inverted, i.e. for a given (s_i, χ_j) we have to find the corresponding r and z coordinates and all the equilibrium quantities needed for the calculation of the coefficients of the variational form (3.19). The code works in dimensionless units such that the major radius R_o, the equilibrium magnetic field B_o, the mass density ρ_o and the Alfvén transit-time R_o/c_A are normalised to their values on the magnetic axis.

3.4.2 Vacuum

The vacuum region contains the antenna and shell surfaces. These are given by arbitrary functions $\rho_a(\theta)$ and $\rho_s(\theta)$ (Fig. 6). The antenna current is specified by the function $\beta(\theta)$ in Eq. (3.22). Different forms of $\rho_a(\theta)$ and $\beta(\theta)$ will define various antenna models: helical, low field side, high field side, both high and low field sides, or top-bottom.

The vacuum contribution (3.31) to the variational form is represented by a matrix and a source vector. These are obtained by calculating Q and Φ_E according to the relations (3.31b). Notice that the boundary and matching conditions are included in these expressions. Everything is then prepared for the calculation of the power delivered by the antenna (3.35): we evaluate Z and $\beta\Psi_E$ according to (3.35b).

3.4.3 Plasma

We have chosen to use finite hybrid elements for the following reasons. Firstly, we want our code to be valid for any aspect ratio, in particular in the cylindrical limit, where we know that regular finite elements may cause trouble due to the spectral pollution (Fig. 3). Secondly, the hybrid elements lead to simpler integration formulas than the regular ones. Nevertheless, they have the same convergence laws. Thirdly, the LION code has been developed from the ERATO stability code which uses finite hybrid elements of first order and it was most con-

venient to retain the same elements.

Let us now describe the principle of the method. Instead of solving the variational form (3.19) as

$$\mathcal{L}\,(X, V) = 0 \quad , \tag{3.44}$$

we consider

$$\mathcal{L}\left(\frac{\partial X^{(1)}}{\partial \chi}, X^{(2)}, \frac{\partial X^{(3)}}{\partial s}, \frac{\partial V^{(1)}}{\partial \chi}, V^{(2)}\right) = 0 \quad , \tag{3.45}$$

with the evident relations

$$X^{(1)} = X^{(2)} = X^{(3)} \quad , \quad V^{(1)} = V^{(2)} \quad . \tag{3.46}$$

An equivalent way to write (3.46) is

$$\lim_{\Delta \to 0} \frac{1}{\Delta} \int_{\Delta} (X^{(1)} - X^{(2)})\, dV = 0 \quad , \forall \Delta \subset \Omega \, , \tag{3.47}$$

and the same for the other relations. After discretization we restrict the conditions (3.47) by identifying Δ with a mesh cell. When the number of these cells tends to infinity we recover the initial problem (3.44).

We expand $X^{(1)}$, $X^{(2)}$, $X^{(3)}$, $V^{(1)}$ and $V^{(2)}$ in a set of basis functions. The simplest choice is made, i.e. we require each term in the variational form (3.19) be constant on each mesh cell. The shape of these basis functions is given in Ref. [29]. The integration reduces to a multiplication of the value of the integrand at the centre of a cell by the volume of this cell. We define x_j as the values of X and V on the nodal points. Figure 7 shows their positions in a mesh cell and their local numbering, j = 1 to 6. At the centre of the cell we have

$$\frac{\partial X^{(1)}}{\partial X} = \frac{x_2 + x_6 - x_1 - x_5}{2\,\Delta X}$$

$$X^{(2)} = \frac{x_1 + x_2 + x_5 + x_6}{4}$$

$$\frac{\partial X^{(3)}}{\partial S} = \frac{x_5 + x_6 - x_1 - x_2}{2\,\Delta S} \qquad (3.48)$$

$$\frac{\partial V^{(1)}}{\partial X} = \frac{x_4 - x_3}{\Delta X}$$

$$V^{(2)} = \frac{x_3 + x_4}{2}$$

For each mesh cell we calculate the contribution to the variational form (3.19) using the formulas (3.48). This yields 6 × 6 "local matrices" which have to be added in the proper way to the total matrix $\underline{\underline{A}}$ of the discretized form. This is done by choosing a global numbering of the nodal points. The matrix $\underline{\underline{A}}$ is constructed by blocks of contribu-

tions of s = const cells (Fig. 8). The numbering is non-monotonic in χ and the periodicity in χ is automatically satisfied. The matrix obtained has the structure shown in Fig. 9. It consists of N_ψ blocks which partly overlap; each block is subdivided in 9 subblocks of dimensions $N_{pol} \times N_{pol}$, each subblock is a band matrix of bandwidth 5. We introduce the regularity condition (3.20) on the first block. The vacuum contribution (3.31) is added to the last block. The matrix A is complex and non-hermitian. In the actual version of the code we store the full blocks, not profiting from the many zeros they contain. However, it is possible to gain a substantial amount of storage by using sparse matrix techniques. We shall discuss this point later.

3.4.4 Algebra

The problem has been reduced to the determination of the solution of the linear system of algebraic equations

$$\underline{\underline{A}}\,\underline{x} = \underline{b} \tag{3.49}$$

where $\underline{b}$ is the source vector due to the antenna (see 3.31). We decompose $\underline{\underline{A}}$ into $\underline{\underline{L}}\,\underline{\underline{D}}\,\underline{\underline{U}}$ where $\underline{\underline{L}}$ and $\underline{\underline{U}}$ are lower and upper triangular matrices and $\underline{\underline{D}}$ is a diagonal matrix. The solution $\underline{x}$ is then obtained in two steps

$$\begin{aligned} \underline{y} &= \underline{\underline{L}}^{-1}\,\underline{b} \\ \underline{x} &= \underline{\underline{U}}^{-1}\,\underline{\underline{D}}^{-1}\,\underline{y} \quad . \end{aligned} \tag{3.50}$$

The matrices are treated block by block with subsequent input/output operations.

We check the validity of the solution $\underline{x}$ by substituating it into the equations (3.49) and comparing the norm of $\underline{\underline{A}}\underline{x}$ with the norm of $\underline{b}$. In all cases the results agree to 13 digits, hence the matrix A is well conditionned for this elimination procedure. Since the variational form itself can be considered as a power balance relation (see 3.7), and since we solve it exactly, we have found a formulation in which the power balance is exactly satisfied.

3.4.5 Diagnostics

The total power delivered by the antenna, P_a, is evaluated according to (3.35). The total power transmitted through the plasma surface, P_p (3.36), is calculated directly from the source vector and the solution at plasma-vacuum interface

$$P_p = \frac{-1}{i\omega}\ \underline{x}^* \cdot \underline{b} \qquad (3.51)$$

From the solution $\underline{x}$ we reconstruct the variables X and V as well as their derivatives $\partial X/\partial\chi$, $\partial X/\partial s$ and $\partial V/\partial\chi$ according to (3.48). We use the definition of X and V (3.16b) to obtain the components of the wave electric field E_N and $E_\perp$, the expression (3.18) for $\underline{\text{rot}}\ \underline{E}$ to calculate the wave magnetic field B_N, $B_\perp$ and $B_\parallel$ and the Poynting vector S_N, $S_\perp$ and $S_\parallel$. The polarizations of the electric field

$E_{\pm} = E_N \pm iE_{\perp}$ and the Fourier decomposition of the solution in the poloidal angle χ are also computed. The power absorption density P_d (3.38), the Poynting flux $P_S(\phi)$ (3.40) and the power flux $P_e(\phi)$ (3.41) are constructed, and the related power balances (3.42) (3.43) are checked.

We have to be careful in comparing $P_S(\phi)$ with $P_e(\phi)$. According to the finite hybrid elements (3.48), the fields $\underline{E}$, $\underline{B}$ and $\underline{S}$ associated with the wave are defined at the centre of each mesh cell. The comparison between $P_S(\phi)$ and $P_e(\phi)$ has to be done on a surface $\partial\Omega_\phi$ passing through the centres of the cells (Fig. 10). Therefore we have to take into account only one half of the volume of the exterior cells when integrating $P_e(\phi)$.

The real antenna structure can be decomposed in Fourier series in the toroidal angle. For each Fourier component we repeat the calculation presented in sections 3.4.1 to 3.4.5. The total power is simply the sum of the powers of all components.

3.4.6 An application of the LION code to JET

As an illustrative case we show an example of the mode conversion scenario at the ion-ion hybrid resonance in JET. The plasma contains a mixture of deuterium (96.6%) and helium-3 (3.4%). The antenna is on the low field side. Its excitation frequency is such that it matches the cyclotron frequency of helium-3 32 cm from the magnetic axis towards

the high field side. We show here only one toroidal Fourier component (n = 3). The equilibrium is of the Solovev type with an expect ratio of 3, an ellipticity of 1.3 and a safety factor on axis of 1.11. The other parameters are $n_e = 3 \cdot 10^{19}$ m^{-3}, $B_o = 3.5$ T, $R_o = 3$ m, the frequency $\omega/2\pi = 35$ MHz, $\nu = 10^{-2}$. The mesh used in this computation is 100 intervals in the radial direction ($N_\psi = 100$) and 50 intervals in the poloidal direction ($N_{pol} = 50$). This mesh size (5000 cells) is approximately the maximum of what can be handled on a CDC-Cyber 855. It requires 500 seconds of central processor time and 89000 words of central memory. The turn-around time is long due to the many input/output operations.

The contours of the power absorption density are plotted in Fig. 11. Notice that the resonances are located on pieces of magnetic surfaces at specific places along the line $\varepsilon_{NN} - n^2/r^2 = 0$ (dotted line) which usually defines the resonance condition in the WKB approximation. The Poynting vector (Fig. 12) shows a complicated fine structure which results from the superposition of the "incoming" and "partly reflected" waves. The contour plot of the absolute value of one circular component of the polarization of the wave electric field, $|E_+| = |E_N + iE_\perp|$, is shown in Fig. 13. Notice the focalization of the fast wave towards the central regions.

Let us now turn to the various checks of this calculation. Firstly, we have $\underline{\underline{A}}\ \underline{x} = \underline{b}$ to all digits (10^{-14}) which means that the solution of the discretized problem is exact. Secondly, the total powers, P_a (3.35) and P_p (3.36), are equal with an accuracy of 3%. Thirdly, the comparison of the Poynting and power fluxes, $P_s(\psi)$

(3.40) and $P_e(\psi)$ (3.41), is good within 1.5%. This does not mean, however, that we have solved the problem with such an accuracy but merely that we did not make gross errors when programming. There remain errors due to the discretization which can be assessed by convergence studies. This is discussed in the next section.

3.5 Properties of the Computational Model

3.5.1 Preliminary remarks

It is nice to show a result of a numerical code. However, we may address the question of its credibility. In other words, we would like to know - and if possible to measure - to which extent we can be confident in the numerical solution. We have shown in the preceding part that the equations are solved exactly on a given finite number of mesh points. We now have to show what happens to the solution when the number of mesh points is increased, whether the results converge and how. This is done in section 3.5.2.

The other parameter which is still free is ν (see (3.8)). In section 3.5.3 we discuss how the solution behaves with respect to the value of ν and how this behaviour can be interpreted.

From a more physical point of view it is important to determine how the numerical code compares with other models and whether it is able to describe correctly the experiment. These points are discussed in section 3.5.4.

3.5.2 Convergence properties

We shall examine the convergence properties in three different cases. We consider first a single species plasma with no resonant layer inside. The frequency is such that $\omega/\omega_{ci} = 1.5$ on the magnetic axis. We introduce a rather strong damping: $\nu = 0.4$. The equilibrium is of the Solovev type, with an aspect ratio of 10, a circular cross-section and a safety factor on axis of 1. The antenna is located both on the high and low field sides and we consider only one toroidal Fourier component: $n = -4$. The problem is solved on various meshes. We define

$$\begin{aligned} N_{cell} &= N_\phi N_{pol} \\ h^2 &= 1/N_{cell} \end{aligned} \qquad (3.52)$$

We let N_ϕ and N_{pol} vary simultaneously with $N_\phi = 2\, N_{pol}$ and examine the numerical results as a function of h.

For non-hermitian problems solved using finite elements of first order the theoretical convergence law of the solution is linear in h. In our case we have found a mixture of quadratic and quartic dependencies. In Figure 14 the quantities ReP_a and ReP_p (3.36) (3.51) are plotted versus h^4. We see that the convergence is quartic, mixed with a small quadratic dependence which shows up only for very fine meshes. Let us write

$$\begin{aligned} ReP_p &= P_{p\infty} + f_p h^2 + g_p h^4 + 0(h^5) \\ ReP_a &= P_{a\infty} + f_a h^2 + g_a h^4 + 0(h^5). \end{aligned} \qquad (3.53)$$

From Figure 14 we deduce g_p = 17 330 and g_a = 11 500. A plot of $ReP_p - g_p h^4$ and of $ReP_a - g_a h^4$ versus h^2 (not shown) yields the converged values $P_{p\infty}$ = 5.500 ± 0.001 and $P_{a\infty}$ = 5.500 ± 0.001. Notice that even for rather coarse meshes the result is within 1% of the converged value. In Figure 15 the power balance relation $(P_e(\psi) - P_s(\psi))/P_e(\psi)$ evaluated on the outermost cells is plotted versus h^2. A quadratic convergence is observed. We are very pleased to see that the converged value is zero and that even for coarse meshes the balance is satisfied with an accuracy of 0.02%. Other quantities such as the reactive power, the maximum value of the power absorption density, the Poynting vector or the electric field converge quadratically in h (not shown).

We now consider the same plasma as before but lower the excitation frequency so that ω/ω_{ci} = 0.375 on the magnetic axis. This is in the Alfvén wave heating domain. The antenna is helical with n = -6, m = -1. A small damping $\nu = 2.10^{-2}$ is introduced. As shown in Fig. 16(a) the quantity ReP_p converges in 0 (h^4). The quantitiy ReP_a still exhibits a mixture of quadratic and quartic convergences. In this sense ReP_p (see 3.51) is a better evaluation of the resistive power than ReP_a (3.35). Nevertheless, both quantities differ only by 2% even for coarse meshes and they converge to the same value $ReP_{p\infty} = ReP_{a\infty}$ = 3.107 ± 0.001. The reactive power inside the plasma shows the same behaviour (Fig. 16(b)): ImP_p converges quartically to 8.515 ± 0.002 and ImP_a^{plasma} converges to the same value with a mixture of quadratic and quartic laws. The vacuum power ImP_a^{vacuum} converges quadratically to 1.936 ± 0.005. At certain points the value of the wave field converges quartically. An example is given in

Fig. 16(c) where $ReE_N(s = .336, \chi = 0, \phi = 0)$ is plotted versus h^4. In general, however, it converges quadratically as shown in Fig. 17(a) where $ReE_N(s = .585, \chi = \pi, \phi = 0)$ is plotted versus h^2. The power balance $(Pe(\phi) - P_S(\phi))/P_e(\phi)$ converges quadratically to zero (Fig. 17(b)). As in the previous case we have an accuracy of 0.02% even with rather coarse meshes.

In some cases the solution shows a complicated structure, so that the maximum mesh size available is insufficient to demonstrate the convergence properties of the numerical code. There is also the problem of the strong variation of ε_{NN} and ε_N (3.5) around the line $\omega = \omega_{ci}$ specially if the concentration of the corresponding ion species is small. In such cases it is difficult to have enough spatial resolution for a good description of ε_{NN} and $\varepsilon_{N\perp}$. Our choice of the coordinates ϕ and χ is certainly not the best in this respect; however, since the solution often shows much structure in ϕ our mesh will describe it advantageously. As an example we consider a large plasma (JET) containing a mixture of hydrogen (97.4%) and deuterium (2.6%). The equilibrium is of the Solovev type, with an aspect ratio of 3, an ellipticity of 1.3 and a safety factor on axis of 1.11. The magnetic field B_o is 3.5 T and the density n_e is $4 \cdot 10^{19} m^{-3}$. The antenna is on the low field side and its frequency, 27.2 MHz, is such that the cyclotron frequency of deuterium is matched at the centre of the plasma column. A small damping ($\nu = 2.5 \cdot 10^{-3}$) is introduced. The solution is shown in Fig. 18 where the contour lines of the circular left polarization, $|E_+| = |E_N + iE_\perp|$, are plotted. Notice the importance of the magnetic structure. The power absorption occurs predominantly on the intersections of the resonant ϕ-surfaces with the line

$\varepsilon_{NN} - n^2/r^2 = 0$ which is the resonance in the WKB approximation (not shown). The mesh used in the calculation is $N_\psi = 100$ and $N_{pol} = 50$ and, as we shall see, is not sufficient to get close to convergence. In Fig. 19 the quantity ReP_p is plotted versus various mesh sizes. Large oscillations occur with an amplitude which decreases with the number of mesh cells. We cannot state an accuracy of better than 30%. Therefore we have to be careful in presenting numerical results such as Fig. 18: they can give a good insight into what happens physically but cannot be regarded as the final (converged) result. An indication that the solution shown may be not so bad is given by the power balance relations. The comparison between the quantities P_a (3.35) and P_p (3.51) gives $ReP_a = ReP_p$ with an accuracy of 0.6%. The agreement between the Poynting and power fluxes, $P_s(\psi)$ (3.40) and $P_p(\psi)$ (3.41), is within 0.5% on the outermost cells and better than 2% elsewhere. However, this does not mean that the solution is so close to the converged result. Satisfying a power balance relation is not sufficient to validate a solution. Let us consider for example the mesh $N_\psi = 48$, $N_{pol} = 24$. We have $ReP_a = ReP_p$ within 1% and $P_s(\psi) = P_e(\psi)$ within 3% on the outermost cells. But the solution is manifestly not correct with such an accuracy (see Fig. 19)!

It can be a fastidious task to make such convergence studies for each case. A possibility of getting an idea of the accuracy of a result is to vary the distribution of the mesh cells and look how the different quantities depend on this variation. In cases like in Fig. 18 the number of resonant magnetic surfaces is so large that the number of cells is not sufficient to describe all of them. By changing the distribution of the mesh cells, new resonances may show up while others

may vanish. This can give an idea of the size of the mesh required for convergence.

The results of the above convergence studies can be summarized as follows: either the mesh is insufficient due to the intrinsic complexity of the solution and no convergence law can be evidenced, or the mesh is fine enough and a convergence or even super-convergence is observed, leading to very accurate results. No mathematical explanation of this super-convergence has been found as yet.

3.5.3 Behaviour with respect to ν

Four different types of behaviour of the solution with respect to ν may occur. They can be related to four different physical situations: excitation of a global mode, resonance absorption, both these phenomena occur simultaneously, none of them occurs.

In the case of a pure global mode, the role of ν is the same as that of the electric resistance in an LCR circuit: the power absorption is inversely proportional to ν. If we trace the power as a function of the frequency, a global mode will show up as a peak whose width is proportional to ν and height inversely proportional to ν. The structure of the power deposition is global and does not depend on ν. This is not the case when a resonant surface is present inside the plasma.

In the case of resonance absorption, the role of ν (Eq. 3.8) is to turn around the singularities. The power is then independent of ν for

sufficiently small ν. For a given mesh, however, there is a minimum value of ν below which the effects of the discretization show up. We have to remember that resonance absorption means the excitation of a mode belonging to a continuum, and that this continuum is numerically represented by a finite set of modes (see Fig. 3). The value of ν must be such that at least two discretized modes are simultaneously excited. To illustrate this important feature we consider an Alfvén wave heating scenario with the same parameters as in Fig. 14. We solve the problem on a mesh with $N_\psi = 40$ and $N_{pol} = 20$. The curve (a) in Fig. 20 shows the total resistive power ReP_p as a function of ν. We see that ReP_p is independent of ν for values down to $\nu_{lim} = 10^{-2}$. Below this value the power varies as $1/\nu$, but this does not mean that a global mode is excited. It merely means that the frequency is equal to the frequency of one of the discretized modes of the continuum; below ν_{lim} we excite only this one. The mode is not physical since it depends on the mesh. Therefore one has to be careful before identifying every feature which varies proportionally to $1/\nu$ as a global mode! By varying the mesh it is nevertheless possible to eliminate the ambiguity. An example is shown in Fig. 20 where the curves (b) and (c) represent the total resistive power, ReP_p, corresponding to the same case but solved on different meshes. A mesh with $N_\psi = 40$ and $N_{pol} = 20$ is used; for the curve (c) we accumulate the mesh points around the main resonant surface. For the curve (b) the excitation frequency is situated between two discretized frequencies, so that below $\nu_{lim} = 10^{-2}$ the power drops proportionally to ν. For the curve (c) we excite a discretized mode (as for curve (a)) but the mesh accumulation allows us to lower ν_{lim} down to 3.10^{-3}.

In the case of the excitation of a global mode in the presence of resonance absorption, ν plays both roles described above. This situation is delicate since we have to be sure that the mode observed is physical and not due to the discretization. The presence of a global mode inside a continuum enhances the power absorption. Let us consider a mode conversion scenario in JET with the same parameters as in Fig. 11: a minority of helium-3 in a deuterium plasma. We only change slightly the frequency (32.1 MHz instead of 35 MHz). The total resistive power ReP_p as a function of $1/\nu$ is plotted in Fig. 21. The error bars are due to the lack of mesh resolution (N_ψ = 100, N_{pol} = 50). Therefore we must consider this result as preliminary. For ν down to 10^{-2} we have

$$ReP_p = P_{cont} + P_{global}/\nu \qquad (3.54)$$

For values of ν smaller than 10^{-2} we deviate from this dependency because we start to lose the contribution from resonance absorption. It is therefore not possible to know whether or not, for smaller values of ν, the power is independent of ν (which means that the power due to the presence of the global mode is also resonantly absorbed). The indication of the presence of a global mode when a continuum is also excited is delicate and needs still further investigations. For example, we can calculate the power as a function of the frequency (or the plasma density). A global mode manifests itself as a peak. The width of the peak is proportional to ν and its height above the continuum is inversely proportional to ν, as (3.54) suggests. This kind of study has been applied to the tokamak TCA where such peaks superposed on a continuum have been found experimentally [34]. This point is discussed in the next section.

In the case where neither a global mode is excited nor resonance absorption occurs, the only absorption arises from the damping ν so that the total power is just proportional to ν.

3.5.4 Comparison with other models and with experiment

A very important check of the validity of the numerical scheme is to examine its ability to reproduce the results of other models. We mention here two limiting cases: the cylindrical limit with finite ω/ω_{ci} and the ideal MHD limit ($\omega/\omega_{ci} = 0$) with finite aspect ratio.

For homogeneous plasmas in cylindrical geometry an analytic dispersion relation can be derived, giving the eigenmodes of the fast magnetosonic wave and of the Alfvén wave. A study of the spectrum of these modes for the case $m = \pm 1$ can be found in Ref. [20]. On using the LION code in this large aspect ratio limit we have found the same spectrum as the analytical one.

In the ideal MHD in toroidal geometry we compare the results of our numerical scheme with those of the ERATO code in its version used for the study of Alfvén wave heating [9]. Since our model does not include finite β effects but ERATO does, both calculations yield the same results with a discrepancy of the order of β.

These two checks demonstrate the ability of the LION code to treat both the physics related to finite ω/ω_{ci} and the toroidal geometry.

The final criterion of the validity of a theoretical model is the comparison with experiment. The studies of Alfvén wave heating in the TCA tokamak provide us with a possibility to perform such a check, and even to show a case where the combined effects of the finite ω/ω_{ci} and toroidal geometry are necessary to explain the phenomenon. The experiments have shown the existence of modes, both global Alfvén and subsequent continuum, in a region of the spectrum where none was expected from a cylindrical model. The interpretation of this fact is the toroidal coupling from the antenna excitation structure (here $n = 2$, $m = 1$) to the mode ($n = 2$, $m = 0$). The ideal MHD toroidal model (ERATO) was able to show the existence of the continuum, while the global mode was still absent in the calculations. With our present model which includes also the effects of finite ion-cyclotron frequency (here $\omega/\omega_{ci} = 0.22$) we have found a global mode at the same place in the spectrum as the experiment [21].

4. Limitations and further improvements of global wave codes

The essential limitation of global wave codes is the maximum mesh size which can be treated due to the large memory storage, input/output operations and central processor time required. We have seen that in some cases this maximum is insufficient to allow us to demonstrate convergence. Therefore we have to develop new algorithms having a better efficiency.

In the LION code the full blocks of the matrix $\underline{\underline{A}}$ are stored though they are sparse (Fig. 9). This is due to the fact that the decomposi-

tion of $\underline{\underline{A}}$ into $\underline{\underline{L}}\,\underline{\underline{D}}\,\underline{\underline{U}}$ fills the blocks. There is clearly a need to overcome this handicap. A possibility is to take advantage of the particular structure of the matrix $\underline{\underline{A}}$: the blocks overlap only for the variable X (see Fig. 9). This arises from the fact that V has no derivative in the ψ direction and from the choice of the finite hybrid elements of first order. The variable V appears therefore as "one-dimensional". It is then possible to eliminate it, so that the only subblocks of the matrix $\underline{\underline{A}}$ which must still be stored as full matrices are the overlaps ($\underline{\underline{A}}_1$ in Fig. 9). All the others can be stored as band matrices. The $\underline{\underline{L}}\,\underline{\underline{D}}\,\underline{\underline{U}}$ decomposition is only applied to the subblocks $\underline{\underline{A}}_1$ and $\underline{\underline{A}}_5$. All the other operations are resolutions of linear triangular or banded systems of equations. This technique has been successfully applied to the ERATO stability code [35]. It led to a gain in CPU time and memory storage of the order of 4 and to a gain in disk storage and input/output operations of the order of 10, thus reducing dramatically the turn-around time. For the LION code the expected gains are comparable.

Another class of algorithms, the iterative methods, keep the sparseness of the matrix $\underline{\underline{A}}$ untouched. These algorithms are easily vectorizable. Unfortunately, in our case $\underline{\underline{A}}$ is neither symmetric nor positive definite. When applying a Gauss-Seidel scheme to our problem, the solution diverges after 4 or 5 iteration steps even on a mesh as small as 4 x 4! A possibility is to solve

$$\underline{\underline{A}}^T\underline{\underline{A}}\,\underline{x} = \underline{\underline{A}}^T\,\underline{b} \qquad (4.1)$$

instead of $\underline{\underline{A}}\underline{x} = \underline{b}$ (3.51). The matrix $\underline{\underline{A}}^T\underline{\underline{A}}$ is symmetric and positive definite but its condition, defined as the ratio of the largest to the

smallest eigenvalue, is usually very bad. A very promising scheme is the "incomplete Cholesky - conjugate gradient" method (ICCG) [36] in which incomplete $\underline{\underline{L}}\,\underline{\underline{D}}\,\underline{\underline{U}}$ decomposition of the matrix is performed, thus retaining its sparseness and greatly accelerating the conjugate gradient iteration.

An alternative to the finite element and finite difference schemes is to expand the fields in Fourier series in the poloidal direction [37]. Unlike the toroidal decomposition, the poloidal Fourier components are not independent from each other. Practically, one has to truncate the series to a finite number of terms. Whether or not such a method is competitive depends on the rapidity of convergence with respect to the number of terms in the Fourier series.

In this paper we discussed the toroidal geometry in particular. It is clear that the numerical methods presented here are not restricted to this geometry but in principle can be applied to other two-dimensional configurations such as axisymmetric mirrors [38,39] or straight stellerators [32,40], for example.

We have restricted ourselves to the cold plasma model. There remains the question of introducing more physics into the numerics. For example, without touching the differential structure of the equations we can model the collisional or ion-cyclotron damping of the fast wave. However, as soon as more effects of finite temperature are taken into account, the differential structure of the equations is altered and thus the code needs more profound modifications. First of all, one would have to derive the pertinent equation in two-dimensional geome-

try, a task which is not easy at all. Moreover, since we met spatial resolution problems already with the cold plasma model, one can expect these problems to be even tougher when "kinetic" short-wavelength waves are present. For more details concerning the global wave solution in warm plasmas see Refs. [22,41].

5. Conclusion

In this paper we have presented and discussed some of the methods which are used for the numerical determination of the global solution in cold plasmas. We hope we have demonstrated that the global wave codes can be a powerful and reliable tool for the study of RF wave heating. A great advantage of these methods is that the accuracy of the results can be checked and measured by doing convergence studies.

As an example we have shown in detail the numerical code LION which solves the pertinent partial differential equations in exact toroidal geometry using a finite element method. The model is valid for any aspect ratio and any shape of plasma cross-section. It provides a description of both the Alfvén and ion-ion hybrid resonances. Its compatibility with the ideal MHD and with an analytic dispersion relation for homogeneous plasma cylinder has been checked. By means of this code we were able to find global modes and to study the toroidal coupling. A successful comparison with the experiment in the TCA tokamak has been made in this context.

The work on global wave codes is still in progress. The efficiency of the methods needs to be improved by adapting modern and if possible vectorizable algorithms to our particular problem in order to increase the maximum mesh size available.

Acknowledgement

The authors wish to thank Drs. T. Hellsten and M. Brambilla for stimulating discussions.

References

[1] K.G. Budden, Radio Waves in the Ionosphere (Cambridge University Press, 1961).

[2] V.L. Ginzburg, Propagation of Electromagnetic Waves in Plasma (Gordon and Breach, 1961).

[3] T.H. Stix, The Theory of Plasma Waves (McGraw-Hill, New York, 1962).

[4] F.W. Perkins, IEEE Trans. Plasma Science PS-12 No 2 (1984) 53.

[5] N.F. Cramer and I.J. Donnelly, Plasma Phys. Contr. Fus. 26 (1984) 1285.

[6] K. Itoh, S.I. Itoh and A. Fukuyama, Nucl. Fus. 24 (1984) 13.

[7] T. Hellsten and E. Tennfors, Physica Scripta 30 (1984) 341.

[8] D.L. Grekov, K.N. Stepanov and J.A. Tataronis, Sov. J. Plasma Phys. 7 (1981) 411.

[9] K. Appert, B. Balet, R. Gruber, F. Troyon, T. Tsunematsu and J. Vaclavik, Nucl. Fus. 22 (1982) 903.

[10] K. Appert, J. Vaclavik and L. Villard, Lecture Notes: An Introduction to the Theory of Alfvén Wave Heating, Lausanne Report LRP 238 (1984) CRPP, Lausanne, Switzerland.

[11] P.L. Colestock, IEEE Trans. Plasma Science, PS-12 No 2 (1984) 64.

[12] R. Behn et al., Plasma Phys. Contr. Fus. 26 No 1A (1984) 173.

[13] M. Brambilla, invited paper presented at this conference.

[14] V.P. Bhatnagar, R. Koch, P. Geilfus, R. Kirkpatrick and R.R. Weynants, Nucl. Fus. 24 (1984) 955.

[15] M. Brambilla and A. Cardinali, Plasma Phys. 24 (1982) 1187.

[16] D.J. Gambier and D.G. Swanson, Phys. Fluids 28 (1985) 145.

[17] K. Appert, R. Gruber, F. Troyon and J. Vaclavik, Plasma Phys. 24 (1982) 1147.

[18] G. Strang and G.J. Fix, An Analysis of the Finite Element Method (Prentice-Hall, Englewood Cliffs, 1973).

[19] R. Gruber and J. Rappaz, Finite Element Methods in Linear Ideal Magnetohydrodynamics (Springer-Verlag, Berlin-Heidelberg, 1985).

[20] K. Appert, J. Vaclavik and L. Villard, Phys. Fluids 27 (1984) 432.

[21] K. Appert et al., Phys. Rev. Letters 54 (1985) 1671.

[22] K. Appert, T. Hellsten, J. Vaclavik and L. Villard, contributed paper presented at this conference.

[24] F. Hofmann, K. Appert and L. Villard, Nucl. Fus. 24 (1984) 1679.

[25] K. Appert, B. Balet, R. Gruber, F. Troyon and J. Vaclavik, Comput. Phys. Commun. 24 (1981) 329.

[26] R. Gruber, J. Comput. Phys. 26 (1978) 379.

[27] K. Itoh, A. Fukuyama and S.I. Itoh, Comput. Phys. Commun. 32 (1984) 35.

[28] P.L. Colestock and R.F. Kluge, Bull. Amer. Phys. Soc. 27 (1982) 8.

[29] K. Appert, B. Balet, R. Gruber, F. Troyon, T. Tsunematsu and J. Vaclavik, Proc. of the 2nd Joint Grenoble-Varenna Int. Symposium, Como, Italy, (1980) 643.

[30] R. Gruber et al., Comput. Phys. Commun. 21 (1981) 323.

[31] K. Appert, G. Collins, T. Hellsten, J. Vaclavik and L. Villard, Proc. of the 12th EPS Conference on Contr. Fus. and Plasma Phys., Budapest 1985.

[32] K. Appert, B. Balet and J. Vaclavik, Phys. Letters 87A (1982) 233.

[33] R. Gruber et al., Comput. Phys. Commun. 24 (1981) 363.

[34] L.S. Solovev, JETP 26 (1968) 400.

[35] A. de Chambrier et al., Plasma Phys. 24 (1982) 893.

[36] D.S. Scott and R. Gruber, Comput. phys. Commun. 23 (1981) 115.

[37] D.S. Kershaw, J. Comput. Phys. 26 (1978) 43.

[38] P.L. Colestock, private communication (1985).

[39] A. Goto, A. Fukuyama and Y. Furutani, Proc. of the 12th EPS Conference on Contr. Fus. and Plasma Phys., Budapest 1985.

[40] M.W. Philips and A.M.M. Todd, contributed paper presented at this conference.

[41] A. Fukuyama, N. Okazaki, A. Goto, S.I. Itoh and K. Itoh, Proc. of the 12th EPS Conference on Contr. Fus. and Plasma Phys., Budapest 1985.

[42] A. Fukuyama, invited paper presented at this conference.

Figure Captions

Fig. 1: Cylindrical configuration.

Fig. 2: Basis functions Γ_j for the regular finite elements of first order and representation $\Xi(r)$ of a function with these elements.

Fig. 3: From the right to the left are shown typical polluted and unpolluted spectra ω_i, together with the Alfvén frequencies $\omega_A(r_i)$ at the spatial grid points r_i, in comparison with the exact analytical spectrum. Alfvén modes (A) are shown with circles, fast magnetosonic modes (F) with crosses.

Fig. 4: Toroidal configuration showing the local magnetic coordinate system ($\underline{e}_N$, $\underline{e}_\perp$, $\underline{e}_\parallel$), the polar coordinates (r,z,ϕ) and the toroidal magnetic coordinates (ψ,χ,ϕ).

Fig. 5: Schematic view of the "up-down" transformation defined by eq. (3.10).

Fig. 6: Poloidal cross-sections of the plasma, antenna and shell surfaces.

Fig. 7: A mesh cell with its 6 nodal points and their local numbering. The small square in the centre is the point where the relations (3.48) are defined.

Fig. 8: A set of s = const cells with the global numering of the nodal points for $N_{pol} = 8$.

Fig. 9: Block and subblock structure of the matrix $\underline{\underline{A}}$ for the numbering shown in Fig. 8. The subblock $\underline{\underline{A}}_9$ is the subblock $\underline{\underline{A}}_1$ of the next block.

Fig. 10: Surface $\partial\Omega_\phi$ passing through the centres of the mesh cells where the Poynting and power fluxes, $P_s(\phi)$ and $P_e(\phi)$, defined by eqs. (3.40) and (3.41), are compared.

Fig. 11: Contour lines of the power absorption density for a mode conversion scenario in JET in a deuterium plasma with 3.4% helium-3. The parameters are: $n_e = 3 \cdot 10^{19}$ m^{-3}, $B_o = 3.5$ T, $R_o = 3m$, aspect ratio = 3, frequency = 35 MHz, low field side antenna, $n = 3$, $\nu = 10^{-2}$. The dashed lines indicate where the frequency matches the cyclotron frequencies of deuterium and helium-3. The dotted line is the approximate resonance condition $\varepsilon_{NN} - n^2/r^2 = 0$.

Fig. 12: Poynting vector for the case shown in Fig. 11. The parallel component is not represented.

Fig. 13: Contour lines of the circular left-hand polarization of the electric field, $|E_+| = |E_N + iE_\perp|$, for the case shown in Fig. 11.

Fig. 14: Convergence study of the total resistive power versus $h^4 = 1/N^2_{cell}$ for a strong damping case with no resonance inside the plasma (ω/ω_{ci} = 1.5 on the magnetic axis, ν = 0.4). P_a denotes the power delivered by the antenna (3.35) and P_p the power transmitted through the plasma surface (3.36) and (3.51).

Fig. 15: Convergence study of the power balance $(P_e(\psi) - P_s(\psi))/P_e(\psi)$ versus $h^2 = 1/N_{cell}$ for the same case as in Fig. 14.

Fig. 16: Convergence study of (a) the total resistive power, (b) the reactive power inside the plasma and (c) the electric field at a given point versus h^4, for an Alfvén wave heating case (ω/ω_{ci} = 0.375 on the magnetic axis, $\nu = 2 \cdot 10^{-2}$).

Fig. 17: Convergence study of (a) the electric field at a given point and (b) the power balance $(P_e(\psi) - P_s(\psi))/P_e(\psi)$ versus h^2, for the same case as in Fig. 16.

Fig. 18: Contour lines of the circular left-hand polarization of the electric field, $|E_+| = |E_N + iE_\perp|$, for a mode conversion scenario in JET in a hydrogen plasma with 2.6% deuterium. The parameters are: $n_e = 4 \cdot 10^{19}$ m^{-3}, B_o = 3.5 T, R_o = 3 m, aspect ratio = 3, frequency = 27.2 MHz, low field side antenna, n = 3, $\nu = 2.5 \cdot 10^{-3}$. The dashed line indicates $\omega = \omega_{CD}$.

Fig. 19: Convergence study of the total resistive power versus h^2 for the same case as in Fig. 18. For the maximum mesh size used (N_ψ = 100, N_{pol} = 50) the convergence is not reached.

Fig. 20: Behaviour of the total resistive power with respect to ν for the resonance absorption case. The frequency used for the curves (b) and (c) is slightly different from that used for the curve (a). For the curve (c) the mesh points are accumulated around the main resonant surface.

Fig. 21: Behaviour of the total resistive power with respect to ν for the case of simultaneous excitation of a continuum and of a global mode. The parameters are the same as in Fig. 11 except the frequency = 32.1 MHz.

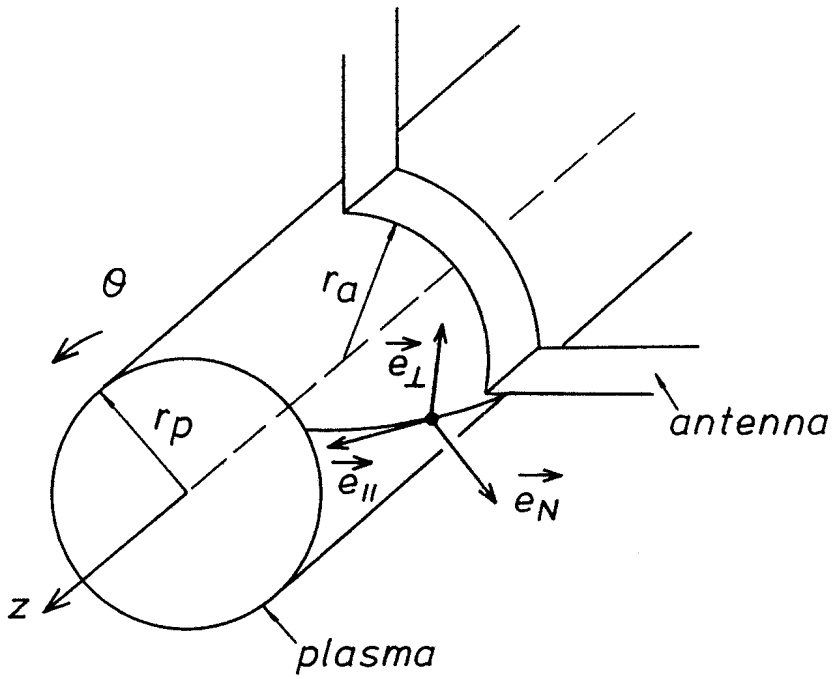
θ
r_a
$\vec{e}_\perp$
r_p
antenna
$\vec{e}_{||}$
$\vec{e}_N$
z
plasma

FIG. 1

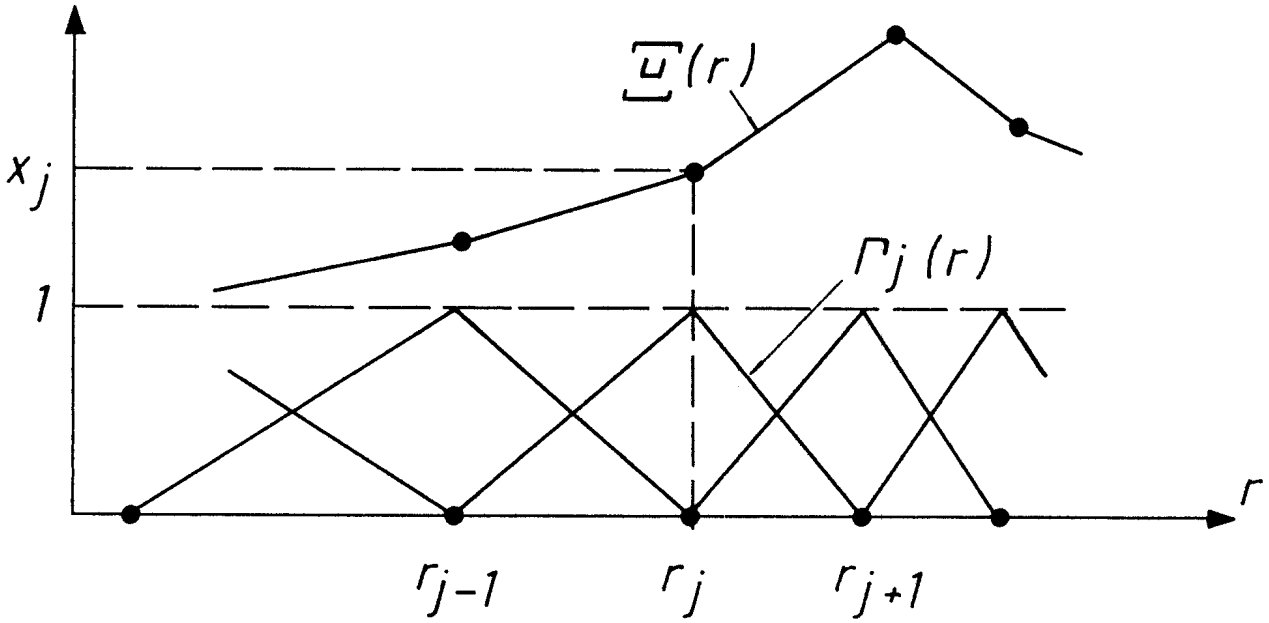
$\Pi(r)$
x_j
$\Gamma_j(r)$
1
r
r_{j-1}
r_j
r_{j+1}

FIG. 2

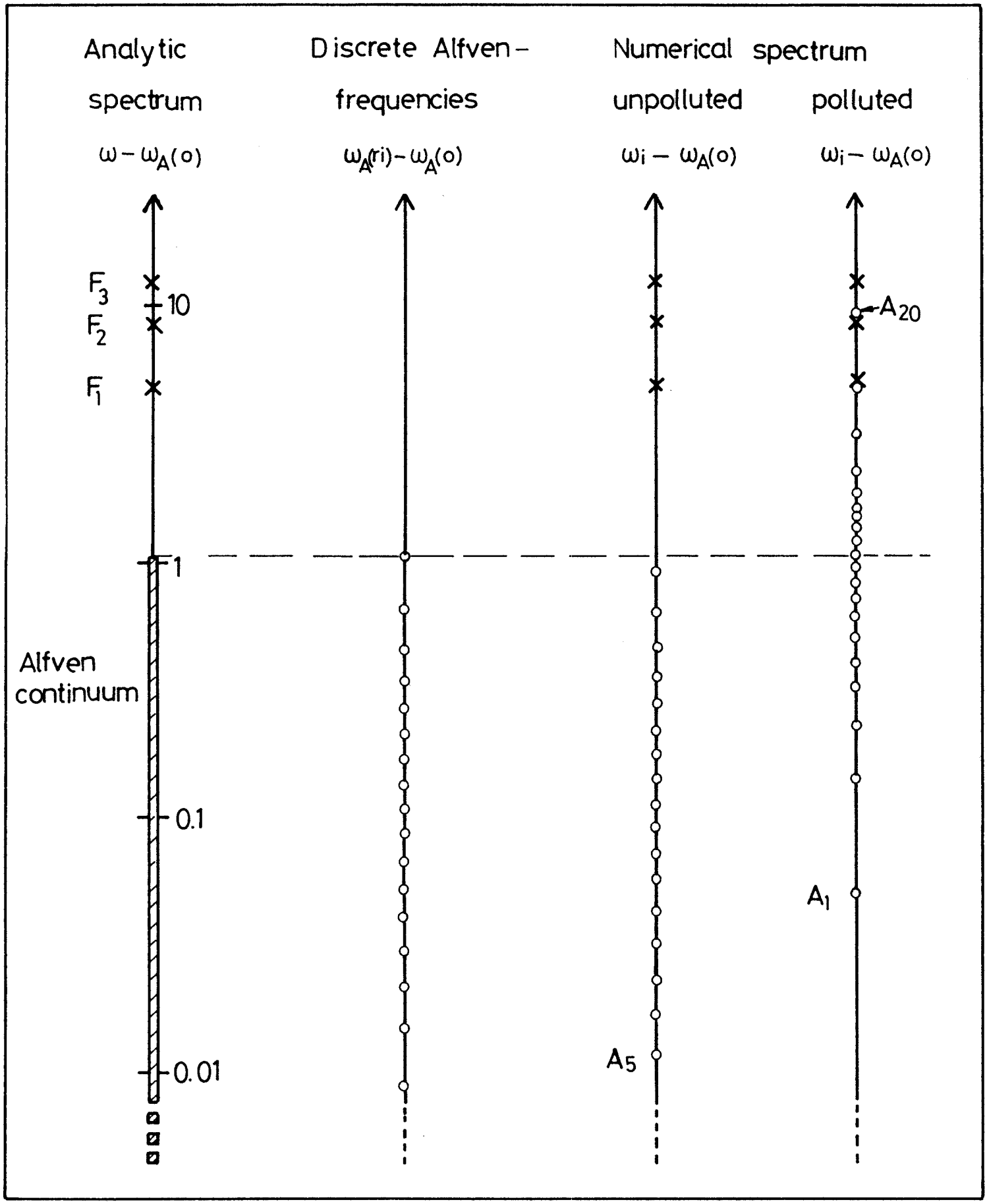
Analytic spectrum
Discrete Alfven-frequencies
Numerical spectrum
unpolluted
polluted
ω − ωA(o)
ωA(ri) − ωA(o)
ωi − ωA(o)
ωi − ωA(o)
F3
F2
F1
10
1
0.1
0.01
Alfven continuum
A20
A1
A5

FIG. 3

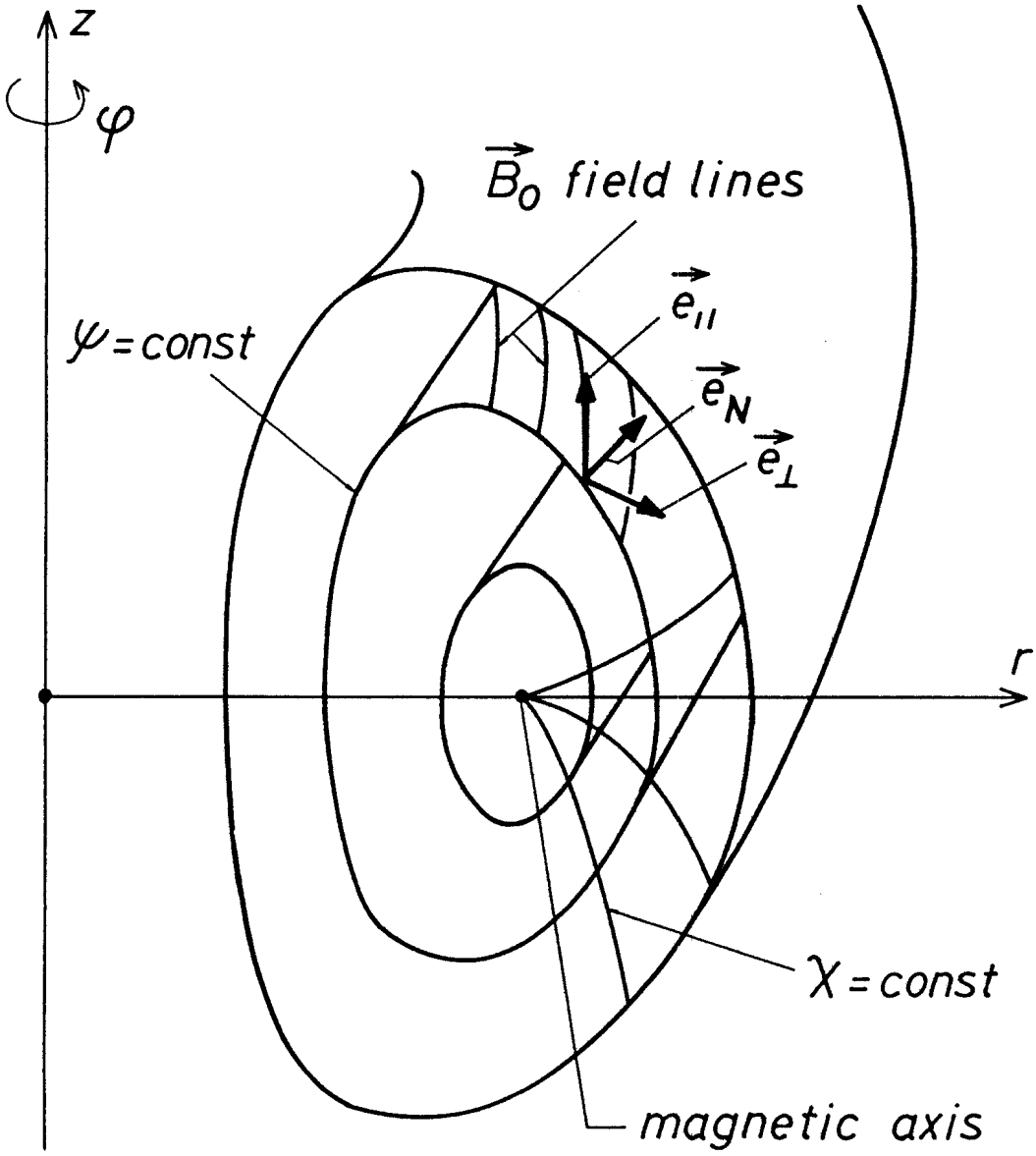
z
φ
$\vec{B}_0$ field lines
$\vec{e}_{\parallel}$
$\vec{e}_N$
$\vec{e}_{\perp}$
ψ = const
r
χ = const
magnetic axis

FIG. 4

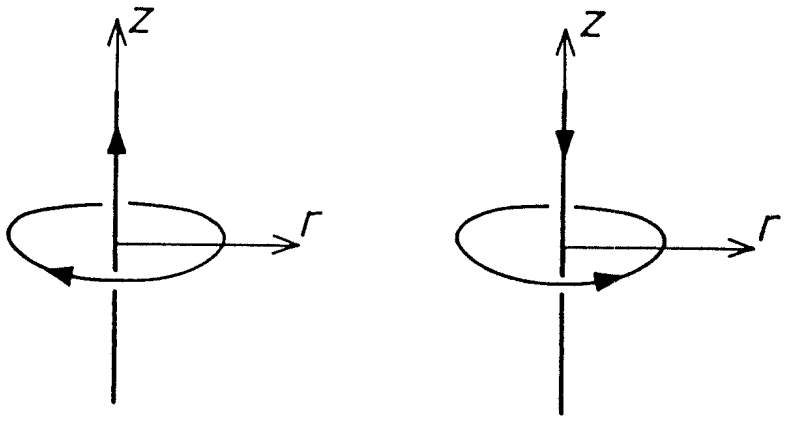

FIG. 5

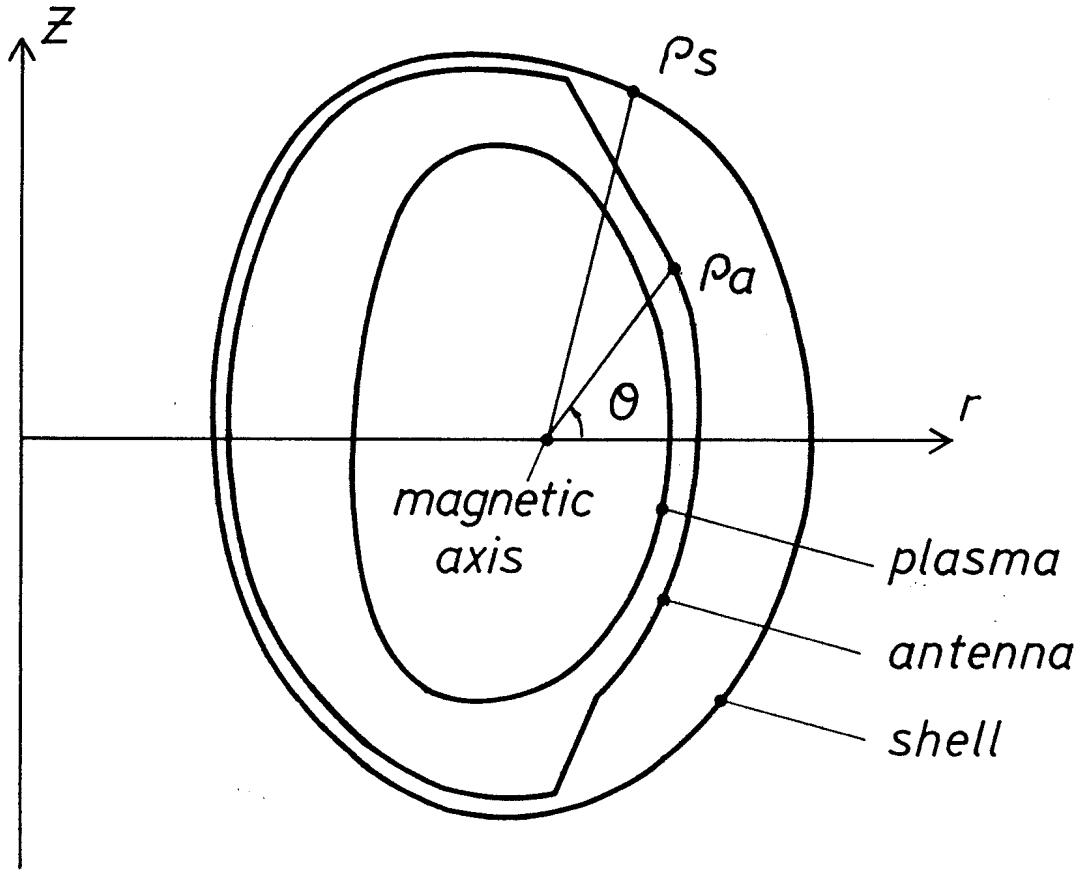

FIG. 6

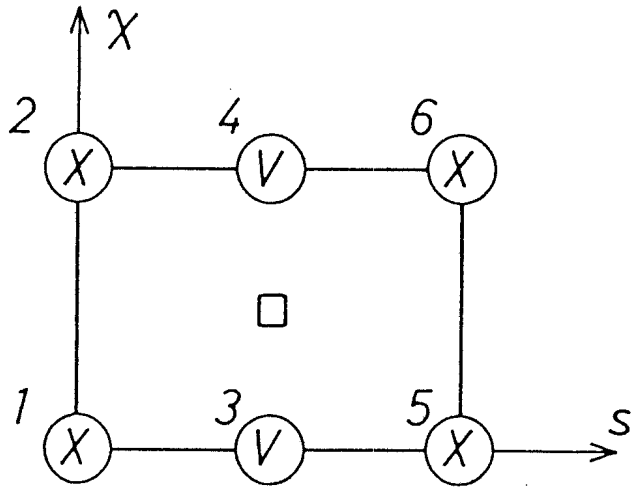
χ
2
4
6
X
V
X
1
3
5
X
V
X
s

FIG. 7

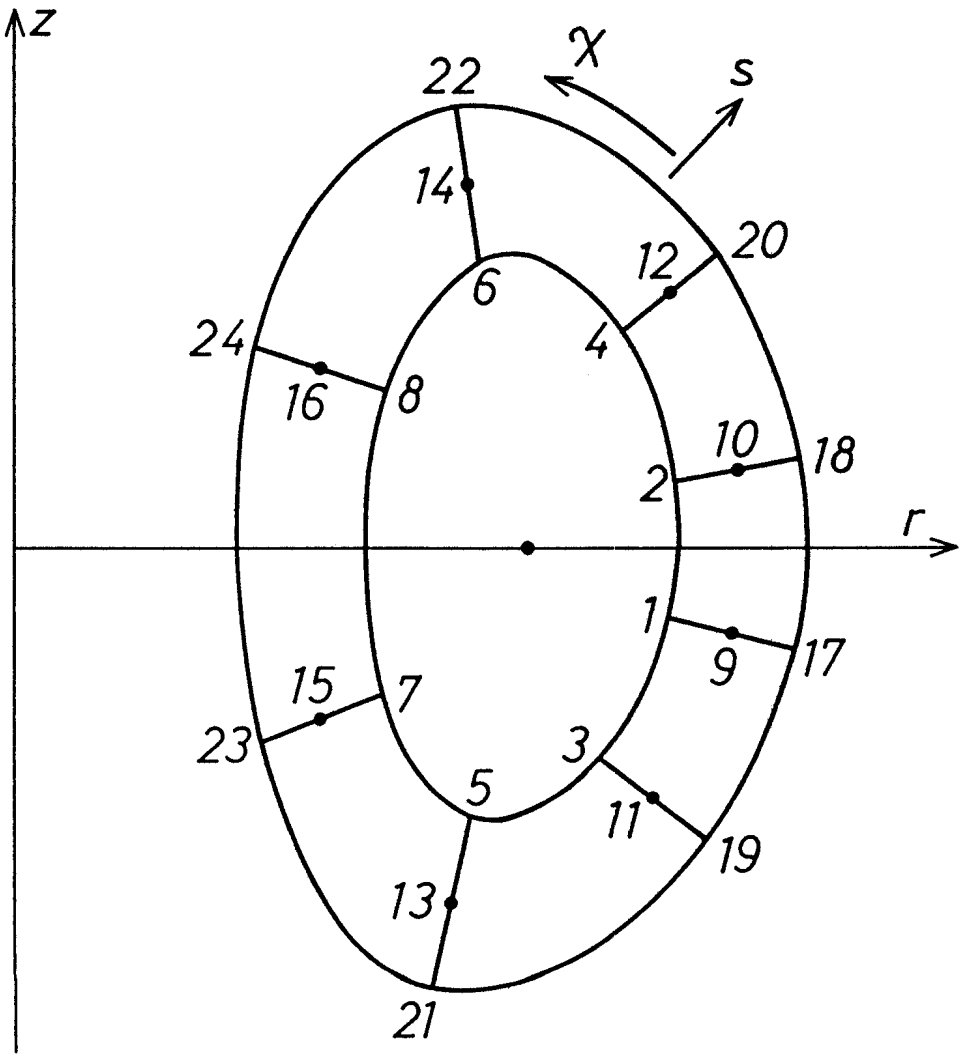
z
χ
s
22
14
6
12
20
24
16
8
4
10
18
2
r
1
9
17
15
7
23
3
5
11
19
13
21

FIG. 8

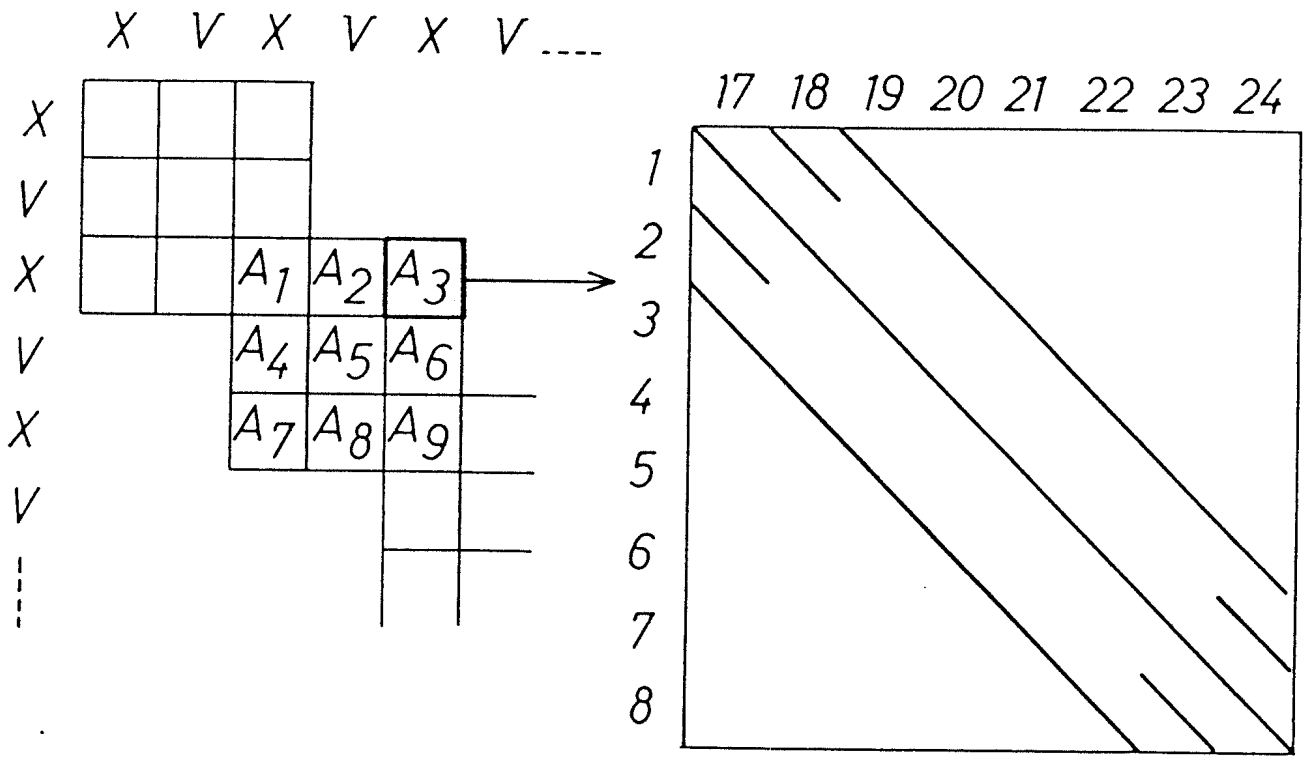
X V X V X V ....
X
V
X
V
X
V
A1 A2 A3
A4 A5 A6
A7 A8 A9
17 18 19 20 21 22 23 24
1
2
3
4
5
6
7
8

FIG. 9

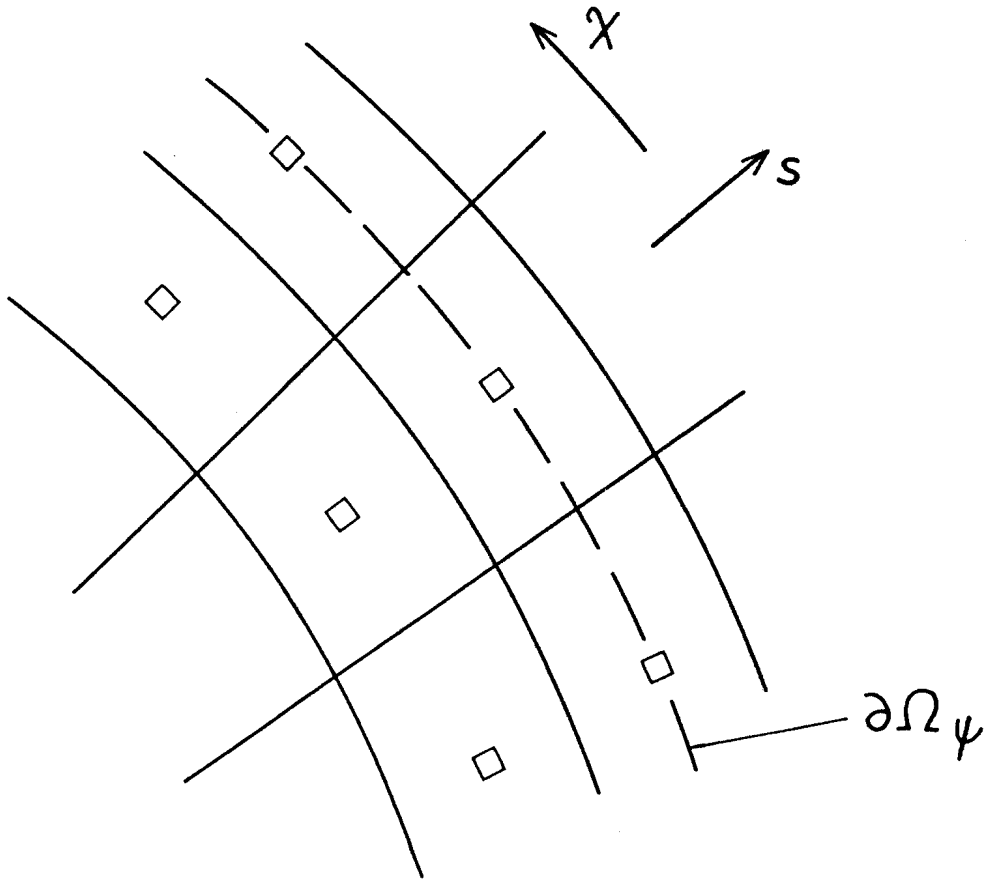
χ
s
∂Ωψ

FIG. 10

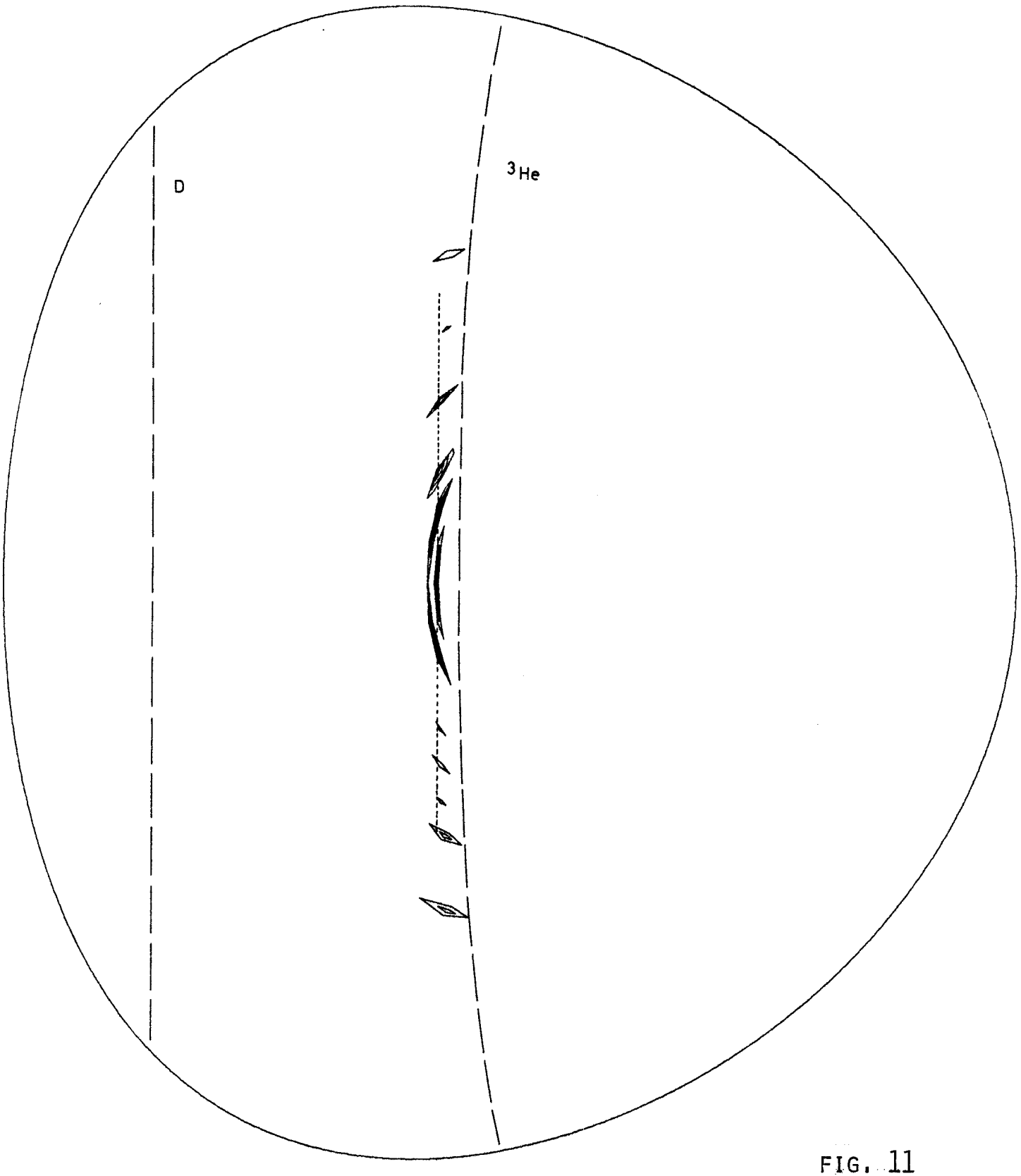

FIG. 11

L-ION POWER ABSORPTION DENSITY
CRPP
LAUSANNE

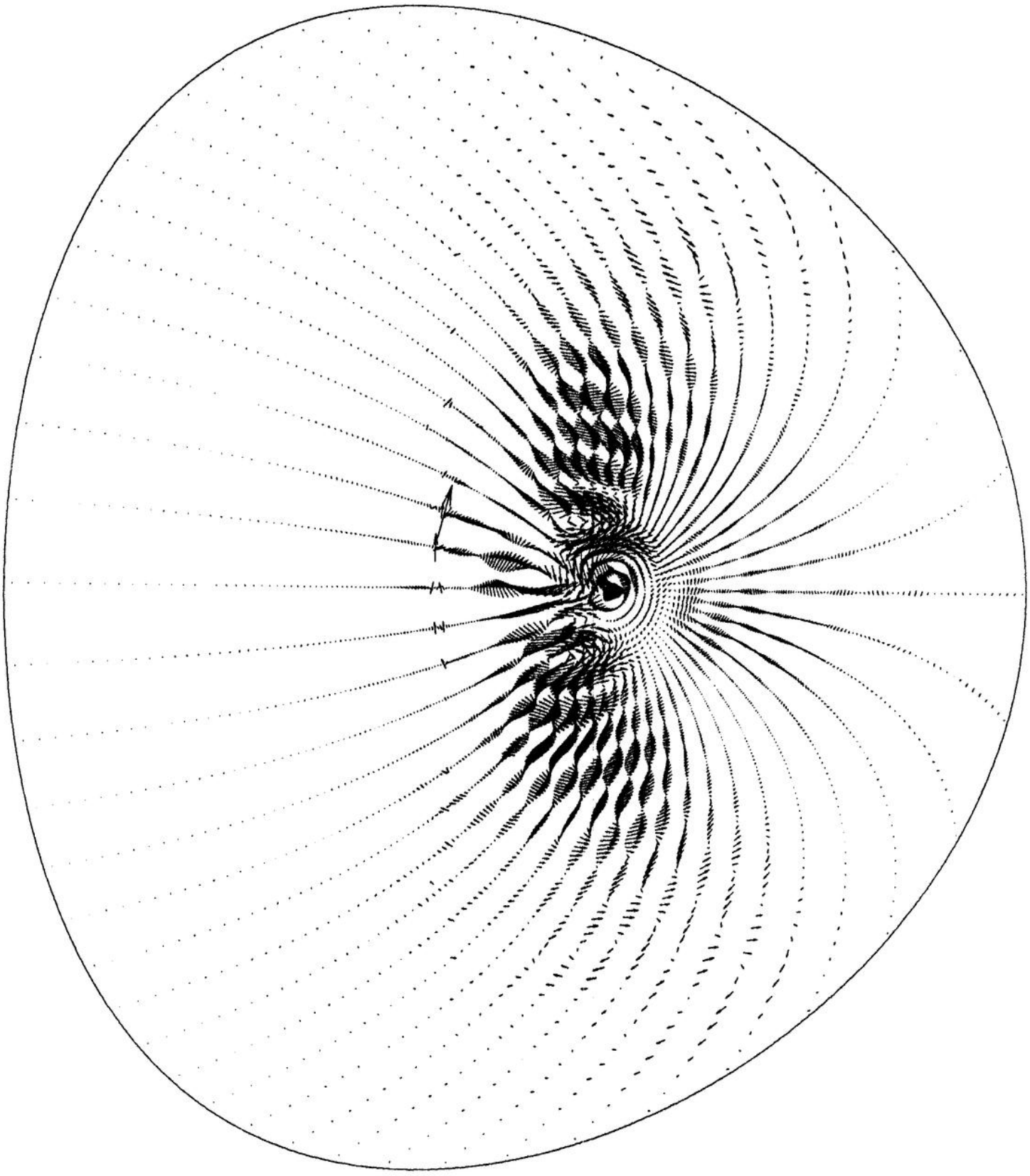

L-ION POYNTING (N, PERP)
CRPP
LAUSANNE

FIG. 12

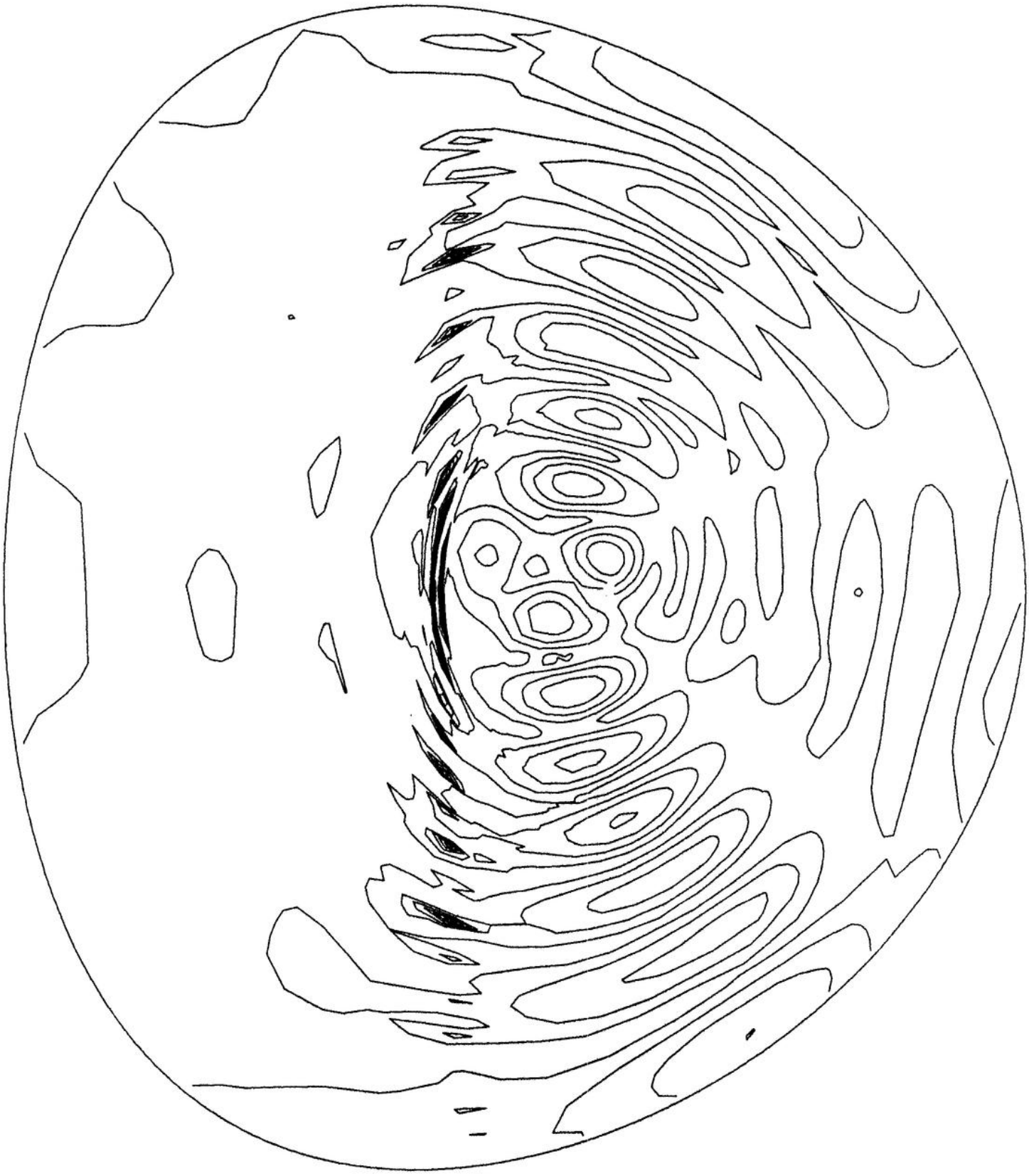

L-ION LEFT POLARISATION

CRPP

LAUSANNE

FIG. 13

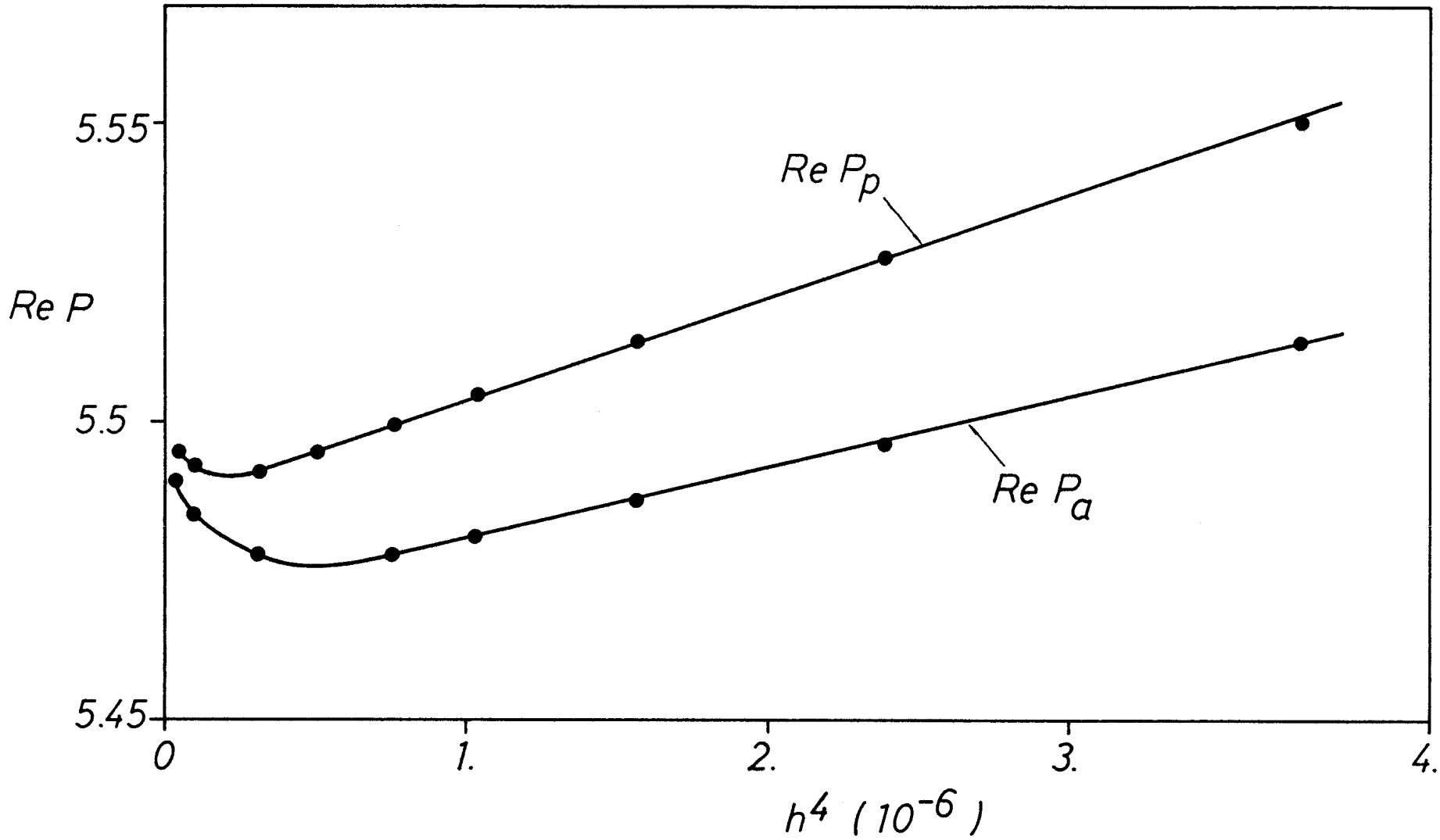

FIG. 14

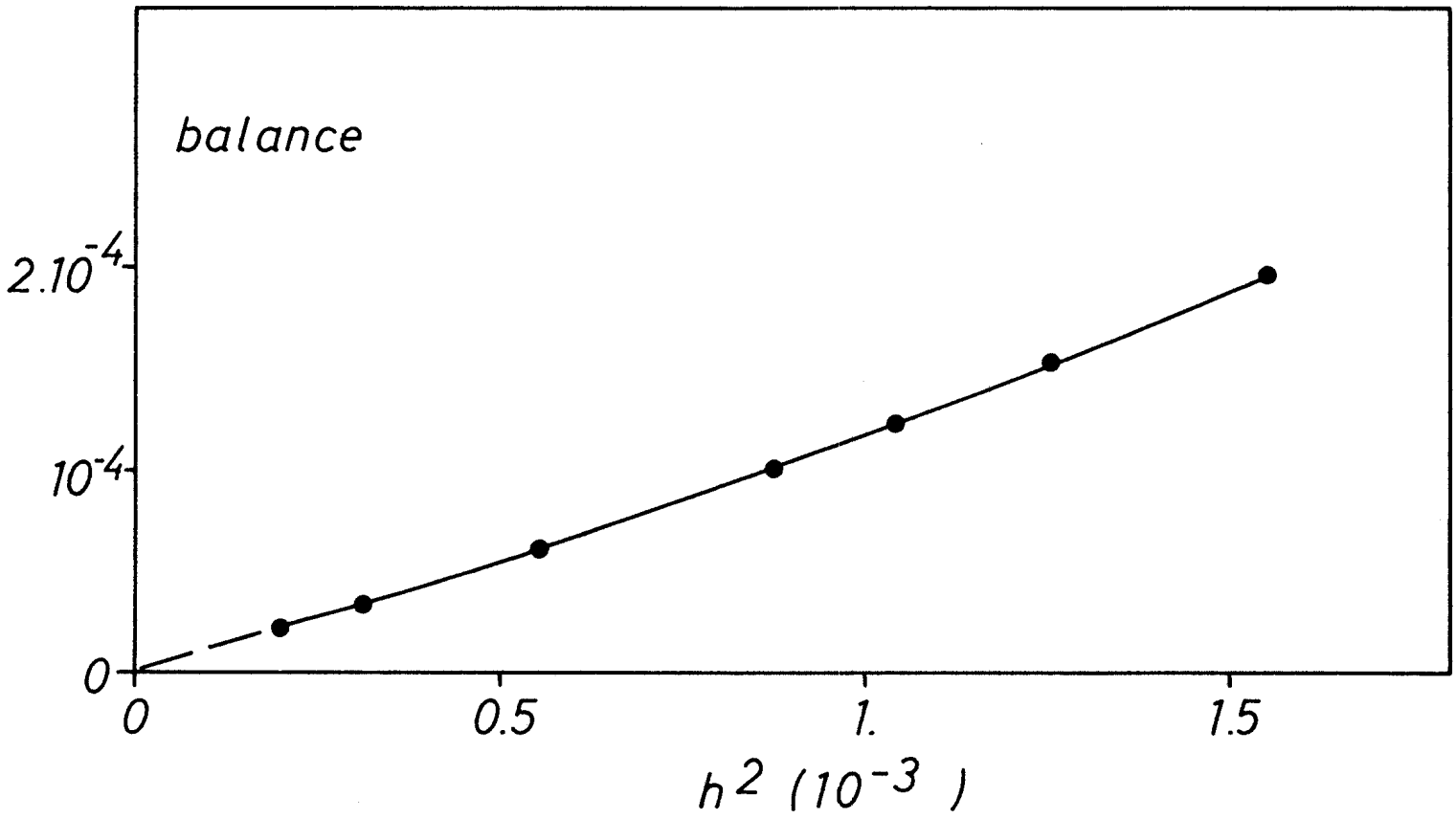

FIG. 15

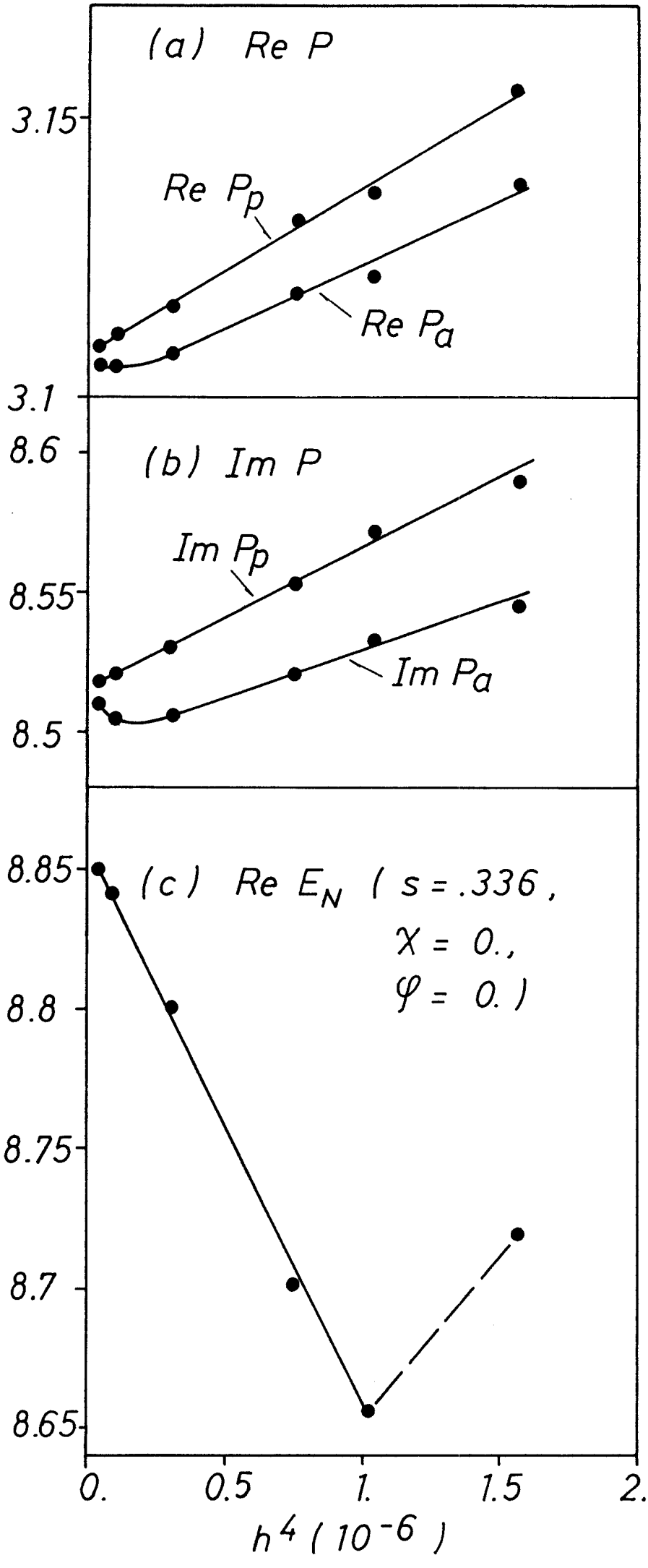
(a) Re P
3.15
Re P_p
Re P_a
3.1
8.6
(b) Im P
Im P_p
8.55
Im P_a
8.5
8.85
(c) Re E_N (s = .336 ,
χ = 0. ,
φ = 0.)
8.8
8.75
8.7
8.65
0.
0.5
1.
1.5
2.
h^4 (10^{-6})

FIG. 16

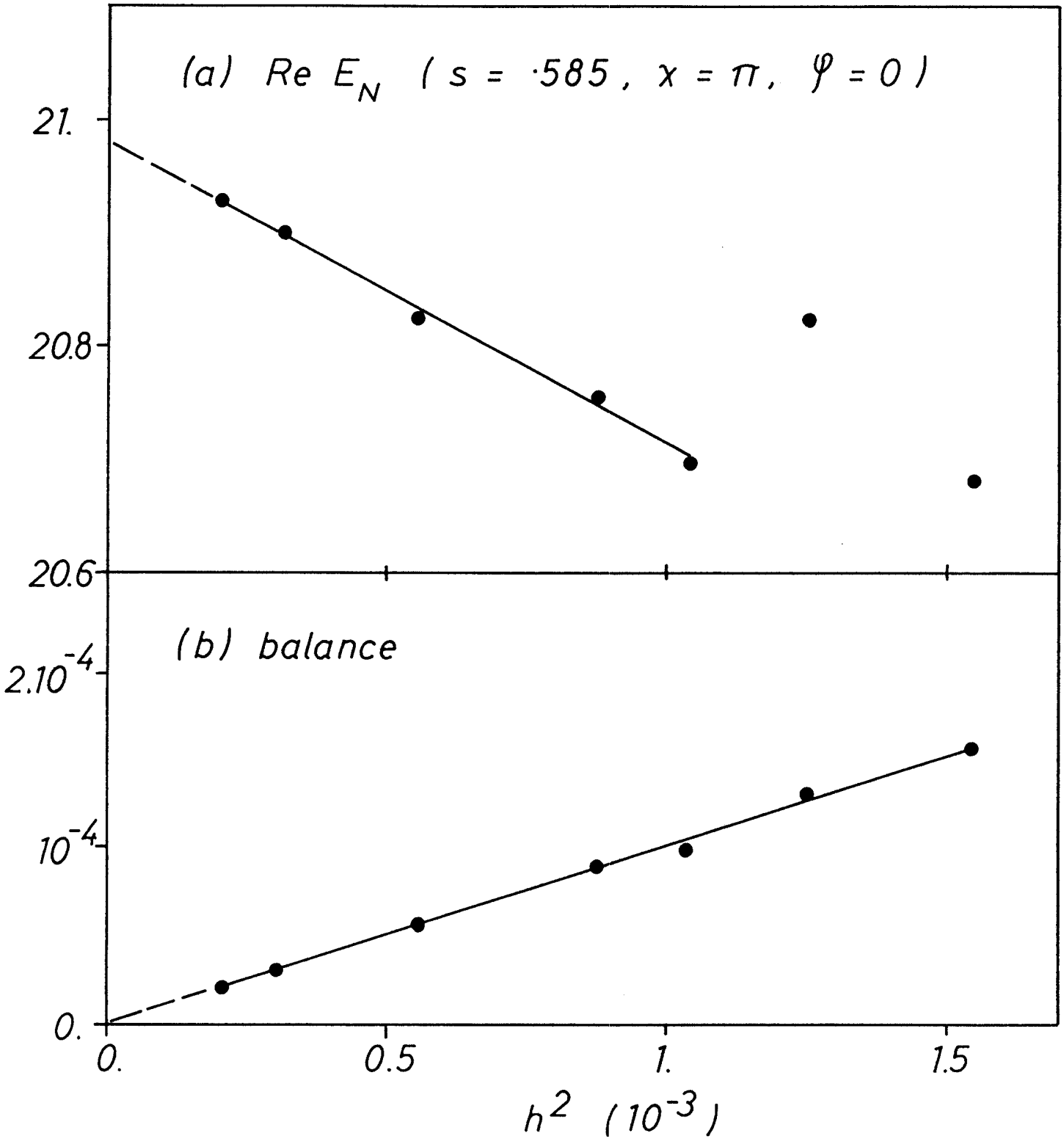

FIG. 17

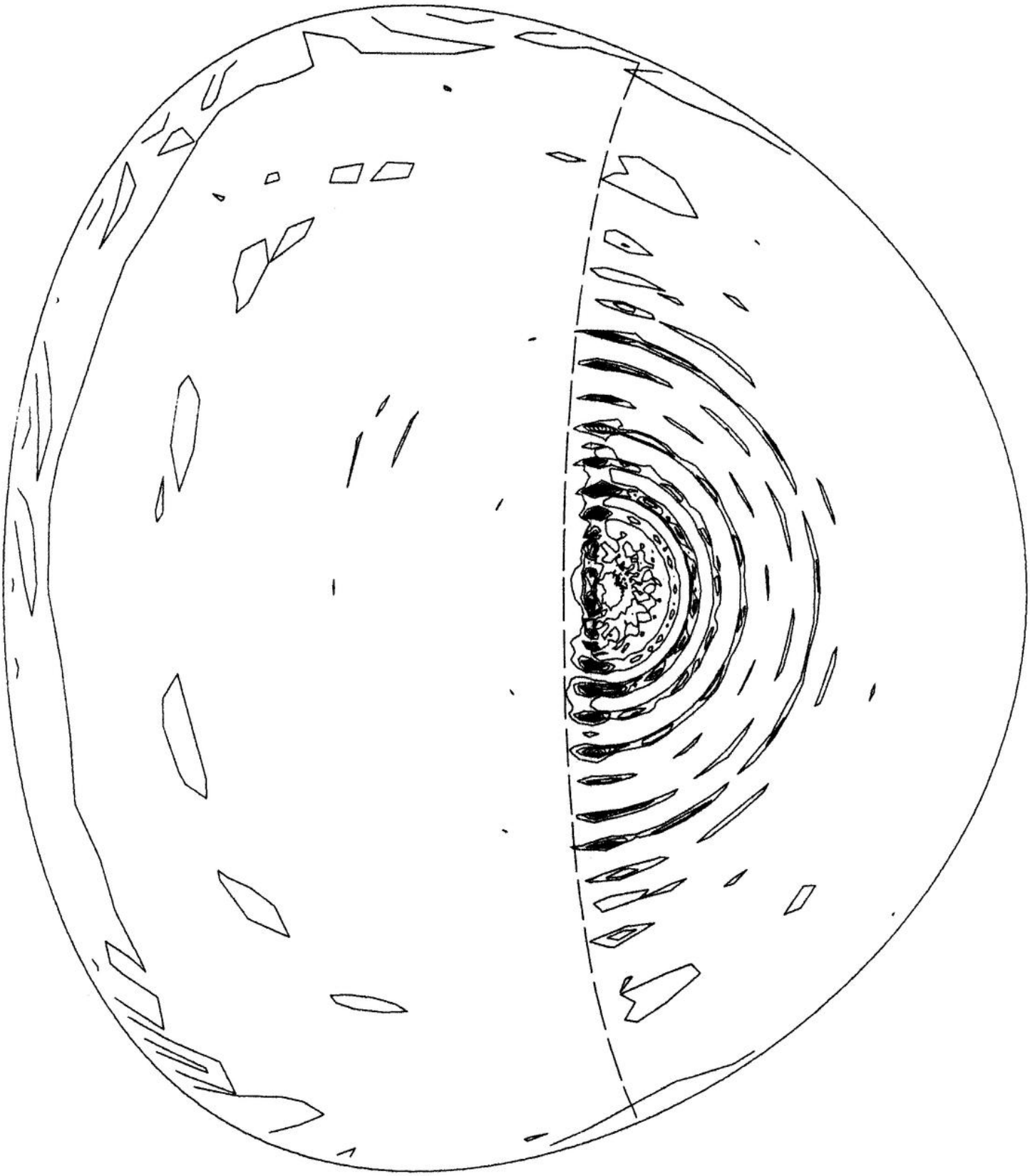

L-ION LEFT POLARISATION
CRPP
LAUSANNE

FIG. 18

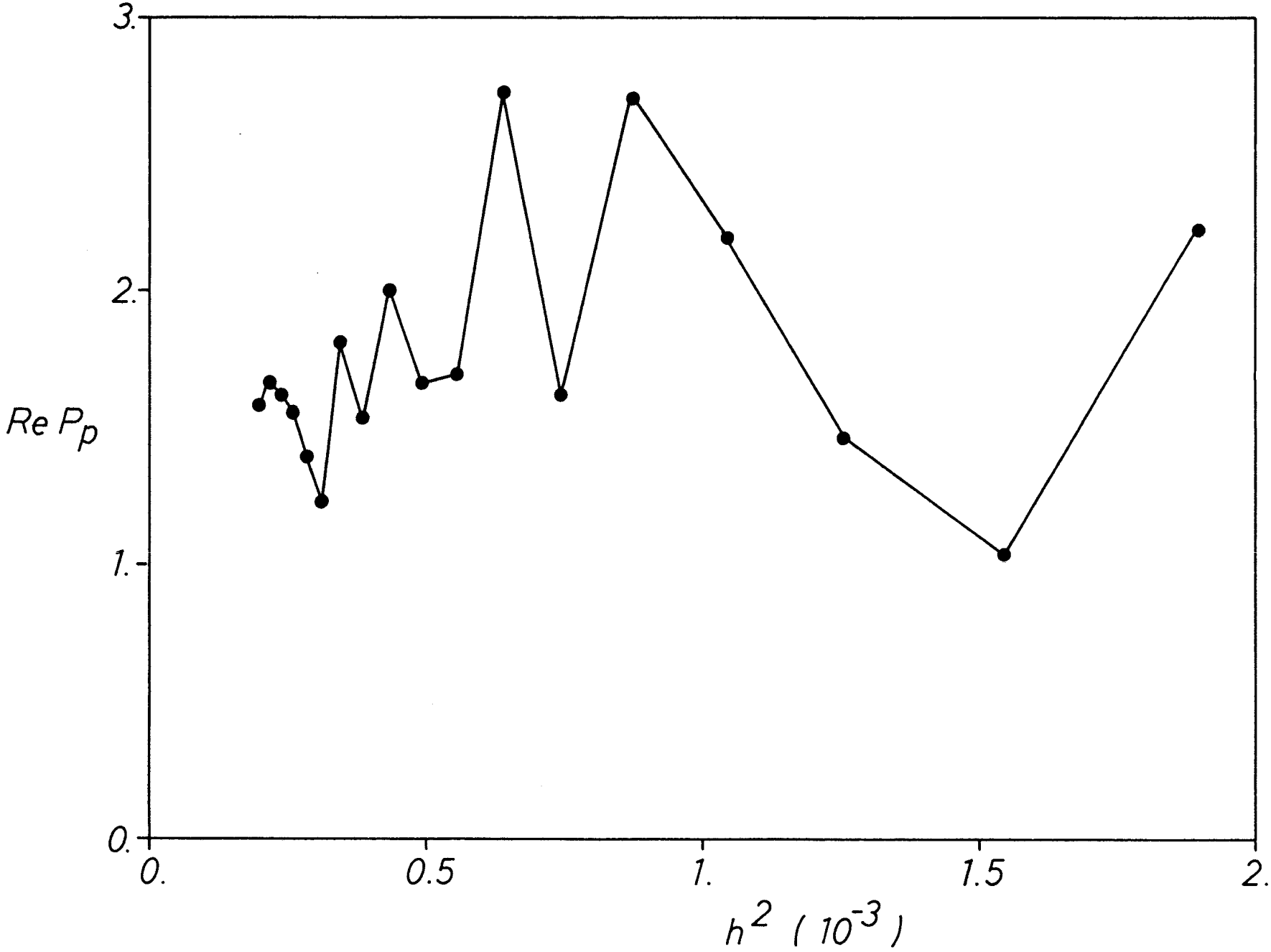

FIG. 19

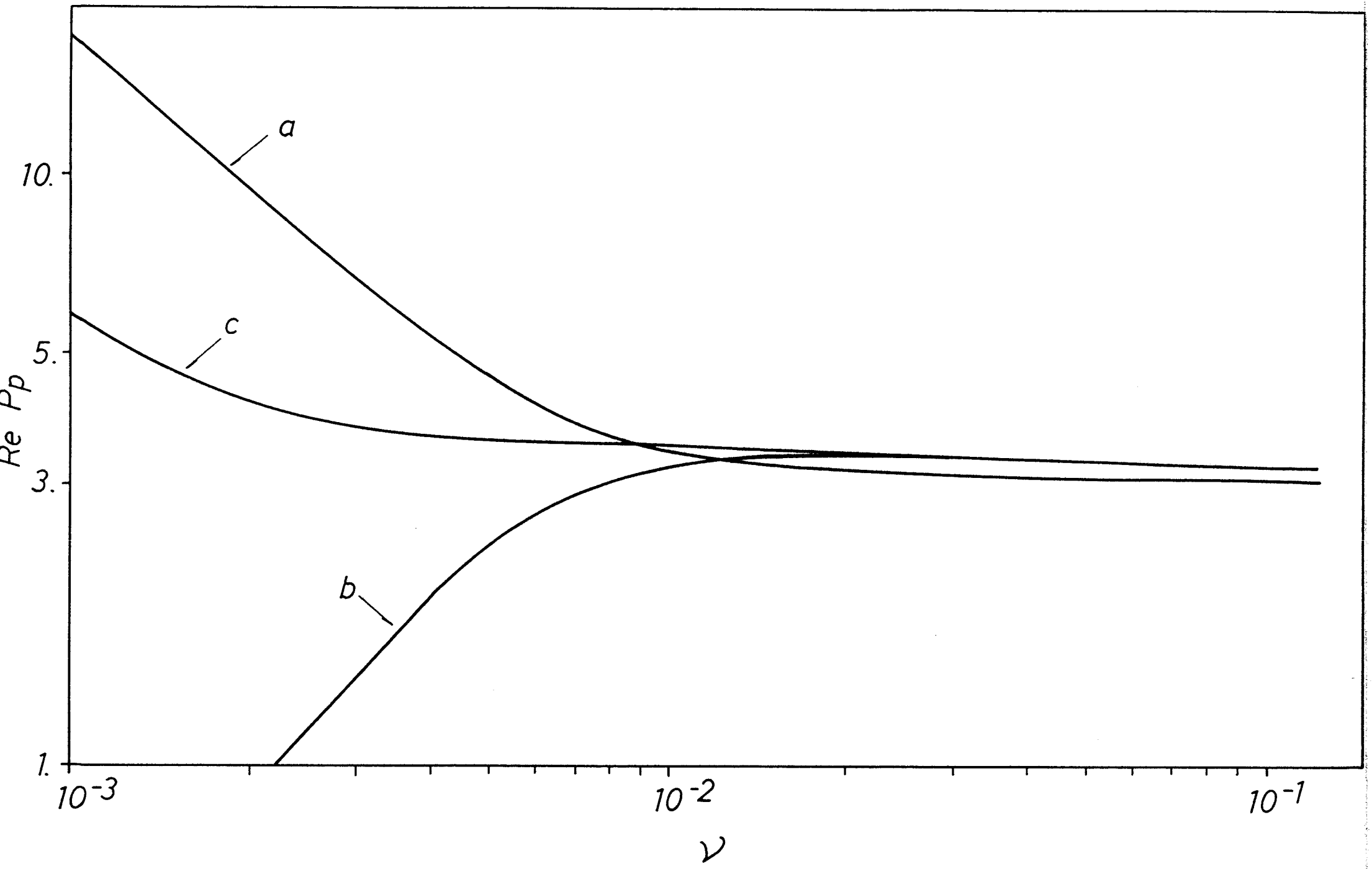

FIG. 20

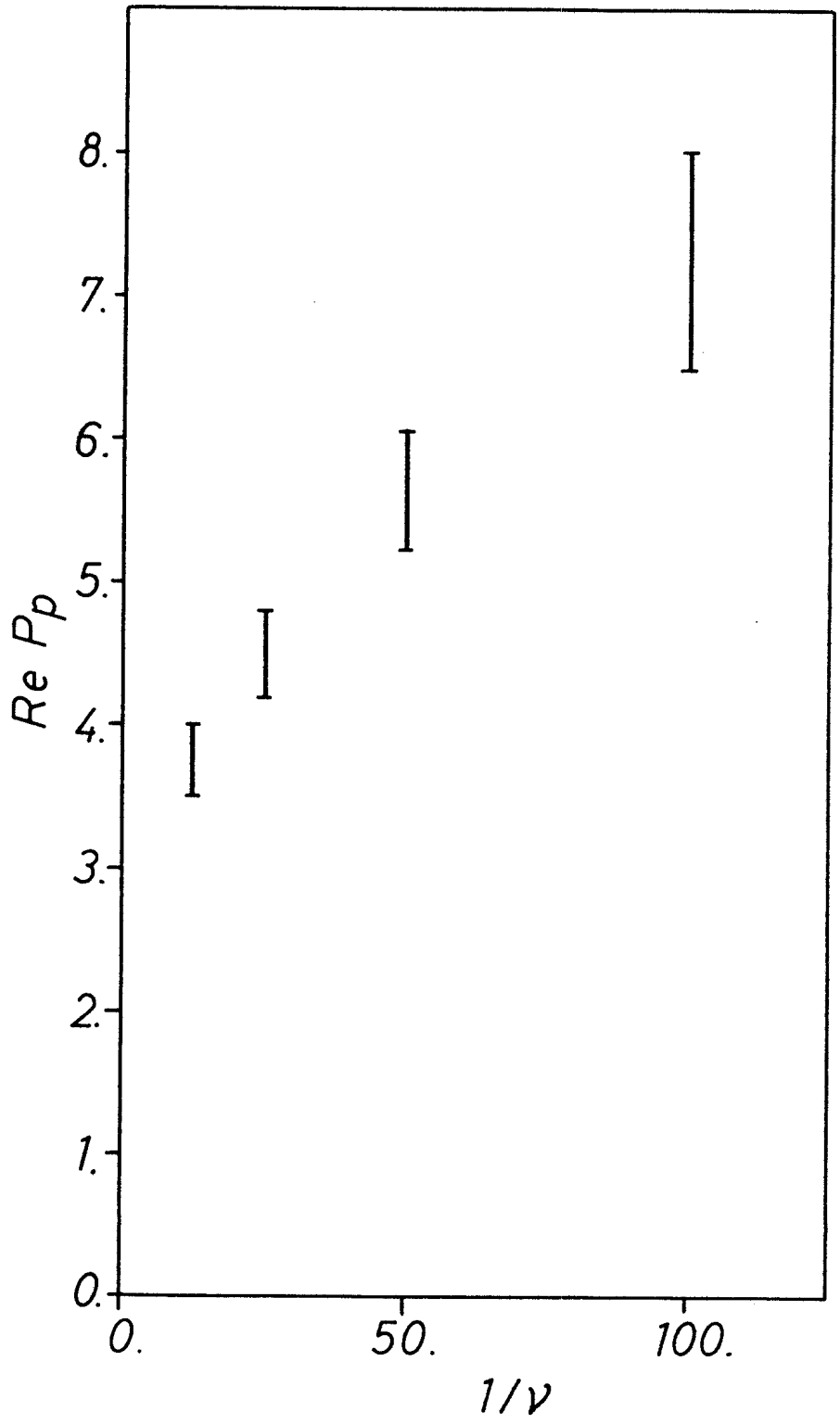

FIG. 21